Valence Electronic Structure of Semiconductor Quantum Dot and Wide Band Gap Oxide Interfaces by Ultraviolet Photoelectron Spectroscopy

A DISSERTATION
SUBMITTED TO THE FACULTY OF THE GRADUATE SCHOOL
OF THE UNIVERSITY OF MINNESOTA
BY

Brooke Andrea Timp

IN PARTIAL FULFILLMENT OF THE REQUIREMENTS
FOR THE DEGREE OF
DOCTOR OF PHILOSOPHY

Xiaoyang Zhu, Advisor

August 2009

Acknowledgements

I would like to thank Kurtis S. Leschkies for providing the CdSe and PbSe quantum dots used in these studies.

This work was supported partially by the National Science Foundation under the NIRT program (CBET-0506672) and partially by the MRSEC Program of the National Science Foundation under Award Numbers DMR-0212302 and DMR-0819885.

Abstract

Energy level alignment is an important factor in efficient charge transfer at an interface between two semiconductors. This topic is explored in model systems that are relevant to quantum dot-sensitized solar cells, inorganic semiconductor nanoparticles adsorbed on single crystal wide band gap oxide substrates, using ultraviolet photoelectron spectroscopy.

Cadmium selenide quantum dots are assembled on a ZnO ($10\bar{1}0$) surface using 3-mercaptopropionic acid linkers. The valence band maximum of the CdSe quantum dots is found to be located at 1.1 ± 0.1 eV above the valence band maximum of ZnO, nearly independent of the size of the quantum dots (2.1-4.2 nm). This finding suggests that, upon adsorption, there is strong electronic interaction between CdSe quantum dots and the ZnO surface. As a result, varying the quantum dot size mainly tunes the alignment of the conduction band minimum of CdSe with respect to that of the ZnO surface.

Sub-monolayer films of PbSe quantum dots are prepared on single crystal substrates, ZnO ($10\bar{1}0$) and TiO_2 (110), and exposed to ligand solutions, either hydrazine or 1,2-ethanedithiol (EDT) in acetonitrile. Interfacial energy alignment is measured as a function of quantum dot size, substrate and ligand treatment. The affect of the ligand treatments on the energy alignment is substrate-dependent. The valence band maximum of the dots is size-independent on ZnO due to strong electronic interactions with the substrate; in particular, EDT-treated films show significant enhancement of quantum dot valence band intensity due to electronic coupling with the ZnO surface. In contrast, the quantum dot valence band maximum is size-dependent and shows a smaller shift between ligand treatments for films on TiO_2, suggesting weaker quantum dot-substrate interactions. In most cases the measured alignment predicts that electron injection from a photoexcited PbSe quantum dot to either ZnO or TiO_2 will necessitate the involvement of higher-lying levels above the first excitonic transition.

Table of Contents

List of Figures

Chapter 1. Introduction

1.1 Quantum Dot Sensitized Solar Cell

The quest for new technologies to produce renewable chemical and electrical energy has spawned tremendous progress in research. Though the development of novel photovoltaics, in which light energy is directly converted into electrical potential, represents just a fraction of the research activity in a substantial field of study, it is an important approach for several reasons. First, the incoming flux of solar photons is inexhaustible and, given the efficiency of currently available photovoltaic devices, well exceeds requirements for the extrapolated need for electricity in the foreseeable future. Second, solar cell modules are very low maintenance once installed, requiring no chemical inputs and having no mechanically moving parts, making them ideal for remote applications or places not presently serviced by electrical grids. Finally, photovoltaics are one of the most expensive sources of electricity per unit energy produced, which is a result of the high temperature and high vacuum processing required in the manufacture of precisely doped, single crystal semiconductor wafers. Significant cost reduction through solution processing of the active device components would make solar electricity more economically viable and, hence, widespread.

The desire to reduce cost of solar electricity production led to study on the incorporation of organic materials, initially dyes and pigments, and the discovery of the excitonic solar cell, which utilizes a fundamentally different mechanism of solar energy conversion than that operating in cells based on the *p-n* junction.[1] In a *p-n* junction (see Figure 1-1) two regions of a semiconductor material are differently doped such that one has excess positive charge carriers (holes) and the other has excess negative charge carriers (electrons). A depletion region forms by way of diffusion of charges toward the interface. Following the recombination of mobile charges near the interface the oppositely charged donor ions remain spatially separated. This creates a built-in electric field that accelerates electrons toward the *p*-type material and holes toward the *n*-type material. Current is created by drift of photogenerated charge carriers away from the interface. In contrast, for an excitonic solar cell the photoexcited state is an exciton, an electron-hole pair that is bound by Coulomb attraction, and an interfacial energy gradient is required for charge separation and generation of current. This section will describe the operation of one type of excitonic solar cell, the dye-sensitized solar cell, review some of the quantum dot systems that have been studied, and discuss Schottky diode solar cells, which have been recently demonstrated for quantum dot systems.

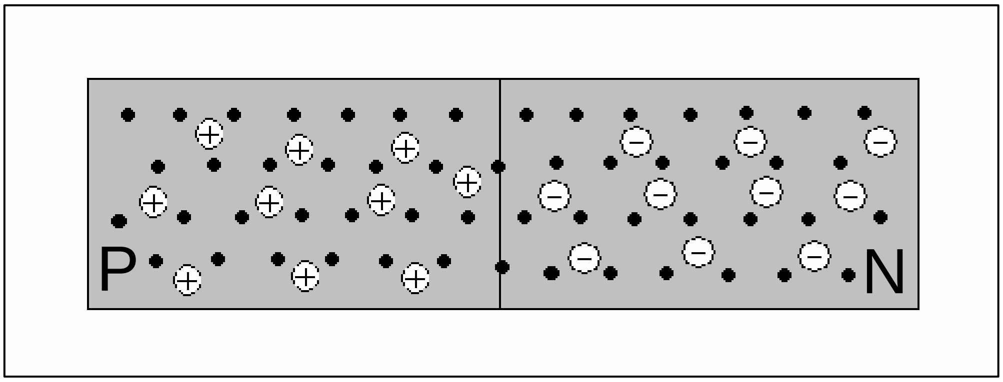

Figure 1-1. Schematic of a *p*-*n* junction. The plus and minus symbols represent excess mobile charges due to dopant atoms.

1.1.1 Concept and Operation

Photoexcitation produces excitons rather than free charge carriers in organic chromophores and semiconductors because of their low dielectric constants and weak intermolecular interactions.[1] Similarly, excitons are produced in semiconductor nanoparticles because of spatial confinement of charge carriers; in fact the Bohr radius of the exciton is the relevant length scale below which quantum confinement effects are observed for any material. The key feature of an excitonic solar cell is that separation of charge carriers, produced upon exciton formation, must take place at an interface between two distinct chemical phases.

The best known example of an excitonic solar cell is the dye-sensitized solar cell, which was reported to exhibit high power conversion efficiencies of around 10% through utilization of a high surface area TiO_2 electron accepting layer.[2] For comparison, average crystalline Si *p-n* junction cells display efficiencies in the 15-20% range.[3] In the prototypical dye-sensitized solar cell, shown as a schematic energy diagram in Figure 1-2, a monolayer of organic dye molecules is adsorbed onto a nanoporous TiO_2 film and immersed in a liquid electrolyte. First, the dye absorbs visible light, promoting an electron to an (exciton-stabilized) excited state. The photoexcited electron is injected into the conduction band of TiO_2 and then diffuses to the collecting electrode. A liquid electrolyte containing a redox couple such as I^-/I_3^- regenerates the oxidized dye molecule and completes the circuit by ionic diffusion. In the ideal case each dye molecule is in direct contact with both the TiO_2 electron accepting material and the electrolyte, allowing charge carrier formation and separation to occur simultaneously; that is, each exciton formed upon light absorption is already at the interface where dissociation occurs.

The energy level alignment at the dye-TiO_2 interface is a critical parameter for efficient exciton dissociation. From the energy diagram in Fig. 1-2 it is apparent that if the excited state of the dye were below the conduction band edge of TiO_2 electron injection could not occur. Optimum alignment requires a balance of multiple factors. For electron injection to dominate it needs to be faster than other relaxation pathways such as radiative or non-radiative recombination. According to Fermi's Golden Rule the transition rate depends on the density of states in the acceptor, as well as the matrix element (coupling strength) between the initial and final states. Within the parabolic band approximation the density of states is zero at the conduction band minimum and increases as $\sqrt{(E - CBM)}$, where CBM is the energy of the conduction band minimum. But shifting the energy levels of the dye molecule up with respect to those of TiO_2, thereby placing the excited state of the dye isoenergetic with more TiO_2 acceptor states, leads to a decrease in maximum photovoltage available from such a cell. The maximum photovoltage is determined by the energy difference between the conduction band edge of TiO_2 and the redox potential of the electrolyte, which must lie above the ground state of the sensitizer (see Fig. 1-2). This thesis work will focus on the topic of interfacial

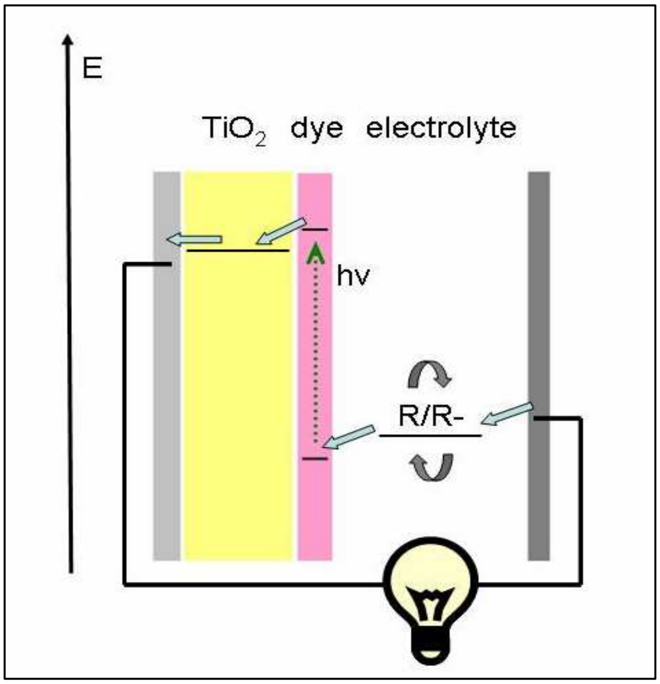

Figure 1-2. Energy diagram of a dye-sensitized solar cell. The arrows indicate the direction of electron current through the circuit.

energy alignment in excitonic solar cells, specifically the quantum dot-sensitized solar cell.

1.1.2 Demonstration and Performance of Quantum Dot Systems

Though the initial demonstrations of the excitonic solar cell used organometallic complexes as chromophores,[2] the potential benefits of incorporating semiconductor quantum dots as visible light-absorbing sensitizers were soon recognized.[4] Spatial confinement of charge carriers in a semiconductor has drastic effects on carrier excitation and relaxation processes. As the particle size decreases, the density of states in any given energy band decreases, ultimately leading to discretization of energy levels and resulting concentration of oscillator strength into more narrow energy windows. Consequently, energy gaps are a function of nanoparticle size, with smaller particles having blue-shifted optical transitions compared with larger particles. In addition to the size-tunable light absorption, quantum dots also exhibit a phenomenon called multiple exciton generation, whereby a single high energy photon can create multiple electron-hole pairs in a process that is conceptually similar to impact ionization, which is depicted schematically in Figure 1-3. The study of the origin and mechanism of multiple exciton generation in semiconductor nanocrystals is a field in its own right,[5] and it will not be discussed in this work. Nevertheless, the implications of multiple exciton

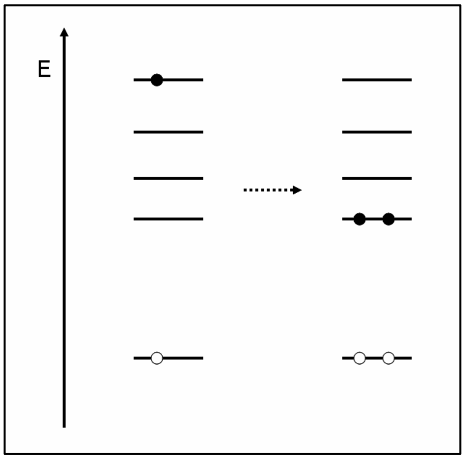

Figure 1-3. Schematic description of impact ionization. Excess energy from one carrier is partially transferred to another through inelastic scattering, leading to more net charge carriers.

generation for enhancement of photocurrent in quantum dot-sensitized solar cells have impelled research in this area.

There are many figures of merit for evaluating solar cell performance. Values such as “power conversion efficiency” (ratio of electrical power output to light power input) depend sensitively on spectral irradiance and device geometry, which is difficult to quantify in nanostructured samples and may vary significantly from sample to sample. Other quantities such as the “incident-photon-to-current-conversion-efficiency”, also known as the “external quantum efficiency” (ratio of # of electrons out to # of photons in, measured as a function of wavelength), do not address conversion of *power*, the product of current and voltage, while measures of “internal quantum efficiency” (ratio of # of electrons out to # of *absorbed* photons) remove losses due to reflectance and spectral mismatch. Though solar cell researchers report various figures of efficiency for their devices, it is important to note that the high end of values of overall power conversion efficiency for quantum dot-sensitized solar cells are currently around 1-2%, which sounds abysmal but is not considerably lower than the ~ 5% benchmark efficiency for solution-processed organic photovoltaics.[6] Clearly, there is a lot of room for improvement in this still very young field.

Initial demonstrations of quantum dots as sensitizers used nanocrystallites deposited on the mesoporous electrode material from an electrochemical bath. Several different material combinations were prepared, including permutations of CdS-, CdSe-, or PbS- on TiO_2, ZnO or SnO_2.[7-10] Electrochemical deposition of nanoparticles is still studied, but others have turned to colloidally synthesized quantum dots, which are superior in terms of their crystallinity, uniform morphology, and monodispersity.[11] During synthesis, long alkyl chain surfactant molecules such as trioctylphosphine oxide or oleic acid are present to mediate particle growth and impart stability to the colloid.[12] Ligand molecules like these bind weakly to the particle surface through carboxylic or phosphonic acid groups and the alkyl tails point outward, promoting solubility in non-polar solvents. However, these ligands are electrically insulating, hindering charge transfer into or out of the particle. The utility of short chain bi-functional linker molecules, containing a functional group at one end to bind to the particle surface (usually a thiol) and a group at the other end to bind to the TiO_2 (usually a carboxylic acid) was later demonstrated. The linker molecules facilitate charge transfer between the two semiconductors, as evidenced by luminescence quenching experiments.[13, 14] This bi-functional linker approach has been used to fabricate quantum dot-sensitized solar cells from a variety of colloidally prepared semiconductor nanoparticles including CdSe,[14, 15] CdTe,[16] InP,[17] InAs,[18] and PbS.[19] In some cases the oxide electrode is pre-treated with the linker molecule, and in other cases a separate solution phase exchange reaction is performed to replace the original ligands introduced during dot synthesis.[20, 21]

In addition to the substitution of semiconductor quantum dots for organic chromophores in these excitonic solar cells, another important modification has emerged: replacement of the nanoparticulate electron-transporting phase with nanowires. Nanowire arrays offer a similar high-surface area platform for quantum dot adsorption as nanoparticle films but are expected to provide a more efficient pathway for electron conduction in delocalized states along the length of the nanowire. In contrast, electron conduction through nanoparticle films occurs via a hopping mechanism and is known to contribute to significant losses in solar cells.[22] Solution-phase syntheses are known for ZnO [23, 24] and TiO_2 [25, 26] nanowires. Oriented, crystalline nanowires can be grown directly on the electrode from nanoparticle seeds and have been found to increase the quantum efficiency of quantum dot-sensitized solar cells.[15, 27]

1.1.3 Schottky Diode Solar Cells

Infrared absorbing quantum dots like PbSe and PbS have been studied more in the context of another configuration that has been realized for quantum dot solar cells: the Schottky diode, where a thin film of semiconductor nanoparticles is sandwiched between two electrodes.[28-30] This design has several features that distinguish it from the previously described quantum dot-sensitized solar cell. The most obvious difference is the lack of a semiconductor heterointerface for charge separation, replaced instead by a Schottky barrier. A Schottky barrier is formed at the interface between a semiconductor and a metal (see Figure 1-4). Panel 1-4 a) shows the interface, here pictured for a *p*-type semiconductor, before contact. Panel b) shows the formation of the Schottky barrier through equalization of the chemical potentials and charge redistribution. In a Schottky solar cell the built in electric field drives the

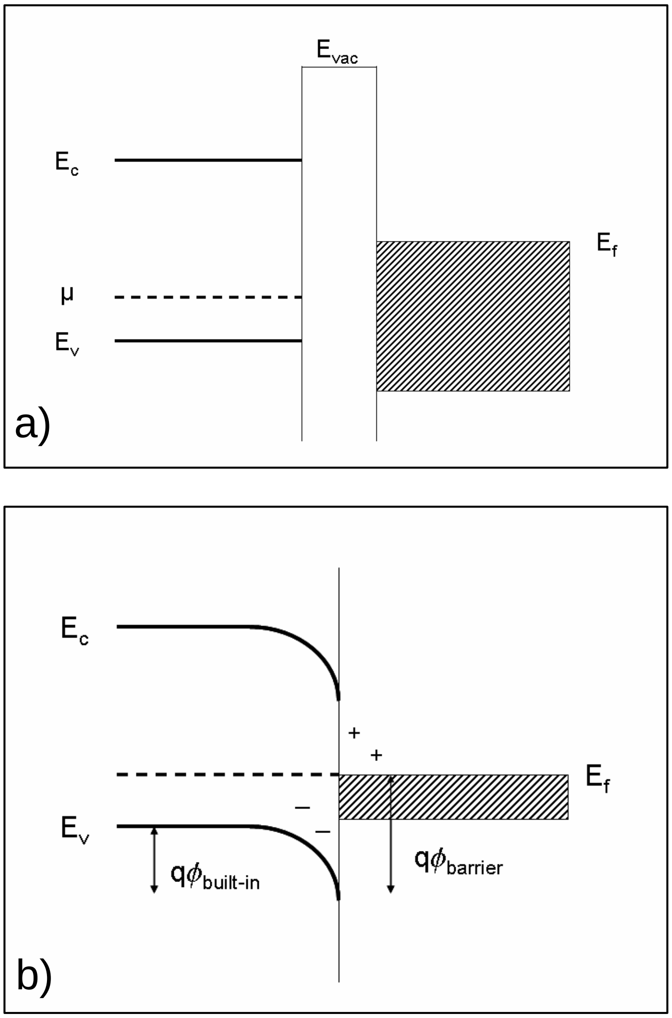

Figure 1-4. Schottky barrier between a *p*-type semiconductor and a metal. a) the interface before contact. E_{vac} is the vacuum level; E_c is the conduction band edge; E_v is the valence band edge; μ is the chemical potential (i.e. Fermi level) of the semiconductor; E_f is the Fermi level of the metal. b) interface after contact. The chemical potentials equilibrate via charge redistribution; electrons are transferred from the metal to the semiconductor. $q\phi_{built\text{-}in}$ is the magnitude of the built-in electric field that drives charge separation. $q\phi_{barrier}$ is the magnitude of the Schottky barrier that provides rectification properties.

separation of photo-induced charge carriers, impelling electrons away from the interface and holes toward the interface (for a *p*-type semiconductor). The Schottky barrier also provides charge rectification; that is, charges encounter an energetic barrier if they attempt to flow against the direction of the built-in electric field. A second major difference between the Schottky diode and the quantum dot-sensitized solar cell is the thickness of the nanoparticle layer. For purposes of sensitization, the absorbing layer should be very close to a monolayer in thickness such that each quantum dot is in contact with both the electron and hole transport phases. For the formation of a Schottky diode, the quantum dot layer has to be thick enough to support band bending and, therefore, exhibit a quasi-solid band structure.

Quantum dots can form ordered superlattices upon solution casting, with roughly spherical particles often showing hexagonal close packing structure. The consequences of this close packing on inter-dot electronic coupling will be discussed in detail in the next section. The following discussion will focus on films of PbSe quantum dots and their modification by ligand treatments, specifically hydrazine and 1,2-ethanedithiol (EDT).

As was mentioned in the previous section, insulating ligands that are present on the quantum dot surface from synthesis suppress charge transfer into or out of the nanoparticle. Hence, the conductivity of solution-cast quantum dot films without any post-synthesis surface treatment is very poor. Film annealing is sometimes used to improve conductivity; it is believed to lead to a combination of partial ligand evaporation and improved alkyl chain interdigitation.[31] Another approach to improving quantum dot charge transfer properties is to introduce a new ligand during or after film deposition, allowing one to tune surface and interfacial interactions through molecular bonding.

In 2005 it was reported that exposing a cast film of oleic acid-capped PbSe quantum dots to a 1 M solution of hydrazine in acetonitrile led to increases in film conductivity of almost 10 orders of magnitude.[32] This dramatic change in electrical behavior was accompanied by a decrease in inter-particle spacing, which was attributed to removal of the oleic acid ligands. The treatment with hydrazine (N_2H_4), a strong base and reducing agent, imparted *n*-type conductivity to the PbSe quantum dot films. It was also observed to be weakly adsorbed to the films, with mild heating to 100˚ C or low milliTorr vacuum exposure resulting in removal of the hydrazine. Further characterization of hydrazine-treated PbSe films noted that although hydrazine exposure caused a red-shift of the lowest energy optical transition, this shift was not due to a growth in size of the quantum dots but rather an increase in the inter-dot electronic coupling.[33] Hydrazine also was not detectable in the PbSe films by (ambient pressure, inert atmosphere) IR absorbance spectroscopy, indicating that very small amounts of the adsorbate (less than a few percent) are sufficient for significant electrical doping.

Treatment of PbSe films with solutions of 1,2-ethanedithiol (EDT), in contrast to hydrazine, has been found to impart *p*-type conductivity to the quantum dot solids.[34] The EDT molecule is also found in high concentrations within the film via IR absorbance and x-ray photoelectron spectroscopy measurements. Like the hydrazine treatment, the EDT treatment leads to a red-shift of the lowest energy optical transition but does not result in growth of the PbSe quantum dots. In fact, the magnitude of the red shift observed in EDT-treated films is slightly larger than for hydrazine-treated films, suggesting that inter-dot electronic coupling is increased in this system. Schottky diode quantum dot solar cells that have been reported used thiol treatments to activate film conductivity.

Ligand treatments such as these offer a simple method to modify the valence electronic structure of PbSe. Optical and electrical characterizations described above suggest that these treatments increase the strength of inter-dot electronic coupling. However, these studies do not address the affect of the treatments on dot-substrate electronic coupling. So far, these ligand treatments have not been applied in the fabrication of quantum dot-sensitized solar cells. In addition, PbSe has not yet been demonstrated in a quantum dot-sensitized solar cell. In Chapter Four the effects of both hydrazine and EDT treatments on energy alignment will be examined for PbSe-ZnO and PbSe-TiO_2 interfaces.

1.2 Electronic Structure of Semiconductor Quantum Dots

In the following section a review of the literature will be presented, discussing electronic properties of the quantum dot materials that are studied in the experiments detailed in Chapters Three and Four. Specific attention will be paid to the evolution of the electronic structure as a function of quantum dot size and the effects of surface ligands.

1.2.1 Cadmium Selenide Quantum Dots

Cadmium selenide is probably the most heavily studied nanoparticulate system to date, owing to advances in synthetic development. In 1993 one of the first reports of monodisperse and crystalline colloids appeared, clearly demonstrating the size dependence of optical transitions.[11] Many modifications of the synthesis have been explored, but the most widely used method is that of “hot injection”, where monomer precursors are rapidly mixed and vigorously stirred in the presence of coordinating solvents for very short times (seconds to minutes). The duration of nanocrystal growth in solution directly correlates with mean particle size, and post-synthetic size-selective precipitation is often used to achieve a narrow size distribution. The availability of high quality sample material has prompted extensive theoretical investigation into the size-dependent and surface properties of CdSe quantum dots.

Knowledge about the evolution of the electronic density of states (DOS) as the size of the quantum dot decreases is important for understanding the behavior of a nanoparticle in a device setting. Wang and Zunger performed early semiempirical calculations for CdSe quantum dots containing up to 1000 atoms and reported DOS for four different dot diameters from 1-4 nm.[35] Compared to the DOS for bulk CdSe, which was also presented, they found that, with decreasing particle size: a) the band gap of the particle increases; b) the width (in energy) of the valence band decreases; and c) peak structure appears in the conduction band. These changes, which occur gradually as the size decreases, can be understood as effects of quantum confinement. An increase in band gap and decrease in valence band width will occur for any spatially confined semiconductor. Consider an energy band formed by delocalization among many states. As states are randomly removed from the band, the width of the band will decrease, resulting in increased transition energies as measured from the band edge. In contrast, the appearance of peak structure at the conduction band edge but NOT the valence band edge, reported by Wang and Zunger, can be qualitatively related to the carrier effective masses in bulk CdSe, which are incorporated into the semiempirical calculation. Effective masses of the electron and hole are obtained by a free electron-like parabolic fit to band structure extrema and expressed as a ratio to the rest mass of an electron. For bulk CdSe the effective mass of the hole is calculated to be as much as 10 times heavier than the effective mass of the electron.[36] Thus, the hole states are less “free”, meaning they are denser in energy and therefore less affected by quantum confinement. This line of reasoning is applied within the effective mass approximation, which is the simplest theory of size-dependent electronic properties. It is important to note that quantitative descriptions can rarely come out of this theory. Single particle tunneling spectroscopy, which can provide an experimental measure of density of states, for 5 nm CdSe quantum dots shows discrete states of comparable width for both polarities,[37] indicating that peak structure is also present in the valence band for CdSe nanoparticles.

In the context of interfacial electronic energy alignment a more fundamental property of the quantum confined system is the relative shift of the band edges with respect to the bulk values, or how the increase in the band gap is split between the conduction and valence levels. According to the (inaccurate) effective mass approximation, one would expect the shift of the conduction band edge to be several times larger than the shift of the valence band edge, in accordance with the different electron and hole effective masses for CdSe. In contrast, the calculations of Wang and Zunger predict that about 45% of the energy shift occurs for the valence band edge over all the sizes studied.[35] And recent experiments utilizing photoemission and x-ray absorption spectroscopy illustrate a roughly equal shift for both valence and conduction levels for CdSe quantum dots in the 1-4 nm range.[38] Cyclic voltammetry measurements also show symmetrical band edge shifts with decreasing dot diameter in this size range.[39] These consistent results on the effects of quantum confinement on the valence electronic structure have important implications for electronic behavior of CdSe nanoparticles in quantum dot-based devices.

But this size-dependence of electronic band structure gives an incomplete picture. As the particle dimensions decrease, the surface area-to-volume ratio increases dramatically, and the effects of the quantum dot surface become more important. As was discussed in previous sections, surface modification of quantum dots with organic ligands serves a variety of purposes. New ligands can be introduced to: improve charge transport properties by removing insulating moieties and reducing tunneling barriers; design solubility for ease of processing; and impart surface functionality for further chemical assembly. Not surprisingly, the manipulation of the quantum dot surface can lead to significant changes in the electrical and optical behavior. Studies on excited carrier relaxation in quantum dots have reported surface termination-dependent relaxation rates and luminescence efficiencies.[40, 41] For instance, thiol ligands on CdSe nanoparticles effectively quench photoluminescence because they serve as traps for holes, preventing radiative recombination.[42]

Surface defect states, which are associated with dangling bond orbitals, are often segregated from the core structure both spatially and on an energy scale. They can trap charge carriers and, due to the presence of distributions and their ability to act as both acceptors and donors, act to compensate charge redistribution at interfaces, contributing to the phenomenon of Fermi level pinning, which will be discussed in the next chapter. However, calculations of CdSe quantum dots show that surface reconstruction and relaxation effectively remove most surface states from the band gap, even in the absence of ligand potentials.[43, 44] Both studies predict the existence of states near the mid gap due to unsatisfied Se atoms. It is useful to note here that most of the commonly used ligands (carboxylic and phosphonic acids, amines, thiols) are known to bind to surface Cd atoms, which can be rationalized using simple electrostatics, and thus it is not surprising that dangling orbitals have mostly Se character.

Puzder *et al.* report that oscillator strengths of optical transitions involving these states are weak, explaining the absence of these features in absorption spectra.[44] The intensity of surface state features relative to the valence band in the calculated DOS differs between the two studies,[43,44] but both calculations place the surface states near the middle of the band gap. In contrast, conductive scanning force spectroscopy measurements of non-ligand-passivated CdSe quantum dots exhibit surface states located within a few hundred meV of both the valence band and conduction band edges that can be reversibly passivated by adsorbed water molecules.[45] Though this type of experiment cannot distinguish the source of the observed surface states, it can point to weakness in the theoretical understanding of real nanoparticle surfaces. In addition, calculations of surface relaxations in CdSe quantum dots usually predict a contraction of surface Cd atoms into the bulk and extension of surface Se atoms outward, even in the presence of ligands, but it has been observed experimentally by x-ray photoelectron spectroscopy [46] and Rutherford backscattering spectrometry [47] that the surface stoichiometry of colloidal CdSe nanoparticles is Cd-rich. The degree of quantum dot surface passivation is strongly dependent on details of sample preparation and is expected to have large effects on device performance.

1.2.2 Lead Selenide Quantum Dots

Interest in PbSe as a nanomaterial has blossomed more recently as a synthetic method for high quality colloidal quantum dots was not reported until 2001.[48] Since then research on PbSe quantum dots has increased considerably. It was the first material for which the phenomenon of multiple exciton generation was demonstrated.[49] Several other unique material properties led to the prediction that PbSe quantum dots would present “the limit of strong quantum confinement”.[50] For instance, bulk PbSe has a very large exciton Bohr radius of 46 nm, so confinement effects can be investigated over a great size range, including a regime with a decreased component due to the surface, since a larger particle has fewer relative surface atoms. The small bulk band gap (0.28 eV at 298 K) facilitates mobility of both electrons and holes, allowing for variation between *n*- and *p*-type electrochemical doping of quantum dot films.[51] Lead selenide is also unique because it crystallizes in the rock salt structure, leading to strong ionic character and highly degenerate band edges.[52] This high degeneracy, combined with low effective masses of both electrons and holes that necessarily characterize low energy-momentum dispersion, leads to very high density of states near the band edges and increased conductance compared to other quantum dot materials.[53] In addition, the high dielectric constant of bulk PbSe ($\varepsilon = 250$) signifies that Coulomb interactions between charge carriers are minimal and that exciton binding energies should be very small.

In particular, the effective masses of electrons and holes are small and symmetric ($m^*_{e-} \sim m^*_{h+} < 0.1$) for bulk PbSe.[54] This has led to the expectation of strong confinement effects for both types of carrier and the presence of a “phonon bottleneck”, wherein hot carrier relaxation is slowed due to large spacing between electronic energy levels and the resulting difficulty of locating a phonon mode of appropriate energy. Such a barrier to nonradiative relaxation would have great consequences for hot carrier extraction and energy conversion efficiency. However, the phonon bottleneck has not been observed experimentally. Lead selenide quantum dots are reported to exhibit intraband relaxation on the same (ps) timescale as bulk PbSe.[55] Recent pseudopotential calculations found that, in addition to the existence of three valence band maxima at different points in **k**-space within 500 meV, the degeneracy (8-fold, including spin) of the main (highest energy) valence band maximum is further broken through loss of translational symmetry and various other coupling mechanisms.[56] The authors conclude that the density of valence band states is much higher than that of conduction states in PbSe quantum dots, thereby providing a mechanism of hole scattering to explain the observed rapid carrier relaxation.

For several of the reasons discussed above, including high carrier mobility and conductance, PbSe quantum dots have been of particular interest in thin film superlattices that act as artificial solids. In close-packed arrays of nanoparticles the electronic wavefunctions that extend beyond the boundary of the particle surface can interact with each other, leading to charge delocalization and an operative reduction of the effects of quantum confinement. Though this discussion will focus on films of PbSe quantum dots, this inter-dot electronic coupling is a general effect and has been reported for other materials such as CdSe [57] and InAs.[58]

Liljeroth *et al.* studied electronic coupling within two-dimensional arrays of PbSe quantum dots using scanning tunneling spectroscopy and found it to strongly affect the measured density of states, reasoning that the low effective mass of PbSe is responsible for extensive wavefunction density outside the quantum dot surface.[31] They reported local variation of the degree of electronic coupling within the array and the existence of two regimes, band-selective and full coupling. The band-selective coupling is manifest as peak broadening of conduction levels while valence levels still maintain distinct peak structure. Given the commonly used argument of equal effective masses for both the electron and hole in PbSe, in addition to the comparatively denser manifold of hole states discussed in detail above, it is surprising that the delocalization is stronger for the electron states. Moreover, scanning tunneling spectra of isolated PbSe quantum dots published by the same group suggest a symmetric shift of both band edges with decreasing dot size, indicating that the valence and conduction levels are equally affected by quantum confinement.[59] The reason for the observation of band-selective coupling is not fully understood, but the authors speculated that non-resonant energy levels of the ligands may be responsible for the increased coupling of conduction relative to valence states. For a considerable minority of sites in the PbSe quantum dot arrays examined by Liljeroth *et al.* strong coupling was detected in both valence and conduction bands, evidenced as step-like structure at both band edges instead of discrete peaks. The density of states profile observed within the full coupling scheme, in combination with strong reduction of the band gap energy, is consistent with electronic formation of a two-dimensional quantum well structure, which exhibits quantum confinement in only one dimension. The authors also performed calculations to elucidate contributions to the electronic coupling in a two-dimensional array and found that particle shape (spherical vs. cubic) and relative inter-particle orientation significantly affect the strength of observed coupling. A recent study by our group showed that electronic coupling between PbSe quantum dots in a two-dimensional array can be tuned by the degree of oleic acid ligand removal, achieved by varying the time of hydrazine treatments.[60] These observations underscore the importance of the particle surface in dictating electronic interactions.

A discussion about the effect of the quantum dot surface is interesting because, in contrast to CdSe, calculations for PbSe predict a lack of surface states, even in the absence of surface passivation by molecular species or ligand potentials.[52, 61] However, these calculations assume a stoichiometric surface. Mass spectrometry and atomic absorption experiments both confirm that the particle surface is Pb-rich, in line with the known mechanism of ligand bonding to Pb sites.[62, 63] In a separate study the authors of Ref. 62 used nuclear magnetic resonance spectroscopy to quantify surface concentration of oleic acid ligands and proposed a model of a stoichiometric nanoparticle core with a surface shell of Pb atoms.[64] Dai *et al.* verified that the surface Pb excess is independent of synthetic conditions such as excessive amounts of Se precursor, nature of the Se precursor or reaction solvent.[63]

The discrepancy between the modeled and actual quantum dot surface has consequences for the interpretation of device performance. It is important to note that electrical transport behavior is often dominated by defects, which can occur at a concentration that is below the detection limit of optical spectroscopies. Transport measurements of annealed PbSe films have shown *p*-type conductivity, which has been attributed to acceptor states due to unpassivated Se atoms, located in the tail just above the valence band maximum.[53] But the nature of surface and trap states in nanoparticle films is quite complex, and the electrical behavior of PbSe quantum dots appears to depend sensitively on subtle changes in adsorbate interactions. In general nanoparticles are very reactive due to their high surface energy. Nanoparticulate materials like PbSe are also sensitive to oxidation in the ambient environment and are usually handled under inert atmosphere. As was mentioned in an earlier section, hydrazine treatment of PbSe quantum dot films led to high levels of *n*-type conductivity.[32] Gradual desorption of hydrazine caused a (reversible) switch to ambipolar and then *p*-type behavior. It has also been noted that treatment of PbSe quantum dot films with other simple amines such as methylamine and pyridine has resulted in p-type conductivity, though these amines were expected to interact with the particle surface by a similar mechanism as hydrazine.[33]

1.3 Organization of the Thesis

This thesis has been organized into four chapters. The first chapter has presented the motivation and scope of the research topic, conceptual background on the quantum dot-sensitized solar cell, and the current theoretical understanding of the nanoparticle materials that were studied. Chapter Two will present the method of photoemission spectroscopy, the preparation of model interfaces that were examined, and the assumptions used in the determination of interfacial energy alignment. Then, in Chapters Three and Four, the experiments that were performed on interfaces of nanoparticles and single crystal surfaces will be described. Specifically, Chapter Three will focus on alignment for CdSe quantum dots on ZnO $(10\bar{1}0)$ attached by a molecular linker, 3-mercaptopropionic acid, and Chapter Four will discuss energy alignment for PbSe quantum dots as a function of nanoparticle size, ligand treatment (hydrazine and 1,2-ethanedithiol) and substrate composition (ZnO and TiO_2).

1.4 References

1. Gregg, B. A., *J. Phys. Chem. B* **2003**, *107*, 4688-4698.
2. O'Regan, B.; Grätzel, M., *Nature* **1991**, *353*, 737-740.
3. Green, M. A., *Prog. Photovolt: Res. Appl.* **2001**, *9*, 123-135.
4. Nozik, A. J., *Physica E* **2002**, *14*, 115-120.
5. Nozik, A. J., *Chem. Phys. Lett.* **2008**, *457*, 3-11.
6. Kim, J. Y.; Lee, K.; Coates, N. E.; Moses, D.; Nguyen, T.-Q.; Dante, M.; Heeger, A. J., *Science* **2007**, *317*, 222-225.
7. Vogel, R.; Pohl, K.; Weller, H., *Chem. Phys. Lett.* **1990**, *174*, 241-246.
8. Liu, D.; Kamat, P. V., *J. Phys. Chem.* ***1993***, *97*, 10769-10773.
9. Vogel, R.; Hoyer, P.; Weller, H., *J. Phys. Chem.* **1994**, *98*, 3183-3188.
10. Hoyer, P.; Könenkamp, R., *Appl. Phys. Lett.* **2005**, *66*, 349-351.
11. Murray, C. B.; Norris, D. J.; Bawendi, M. G., *J. Am. Chem. Soc.* **1993**, *115*, 8706-8715.
12. Puzder, A.; Williamson, A. J.; Zaitseva, N.; Galli, G.; Manna, L.; Alivisatos, A. P., *Nano Lett.* **2004**, *4*, 2361-2365.
13. Lawless, D.; Kapoor, S.; Meisel, D., *J. Phys. Chem.* **1995**, *99*, 10329-10335.
14. Robel, I.; Subramanian, V.; Kuno, M.; Kamat, P. V., *J. Am. Chem. Soc.* **2006**, *128*, 2385-2393.

15. Leschkies, K. S.; Divakar, R.; Basu, J.; Enache-Pommer, E.; Boercker, J. E.; Carter, C. B.; Kortshagen, U. R.; Norris, D. J.; Aydil, E. S., *Nano Lett.* **2007**, *7*, 1793-1798.
16. Cao, X.; Chen, P.; Guo, Y., *J. Phys. Chem. C* **2008**, *112*, 20560-20566.
17. Yu, P.-R.; Zhu, K.; Norman, A. G.; Ferrere, S.; Frank, A. J.; Nozik, A. J., *Langmuir* **1998**, *14*, 3153-3156.
18. Murphy, J. E.; Beard, M. C.; Nozik, A. J., *J. Phys. Chem. B* **2006**, *110*, 25455-25461.
19. Hyun, B.-R.; Zhong, Y.-W.; Bartnik, A. C.; Sun, L.-F.; Abruna, H. D.; Wise, F. W.; Goodreau, J. D.; Matthews, J. R.; Leslie, T. M.; Borrelli, N. F., *ACS Nano* **2008**, *2*, 2206-2212.
20. Aldana, J.; Wang, Y. A.; Peng, X.-G., *J. Am. Chem. Soc.* **2001**, *123*, 8844-8850.
21. Moody, I. S.; Stonas, A. R.; Lonergan, M. C., *J. Phys. Chem. C* **2008**, *112*, 19383-19389.
22. Frank, A. J.; Kopidakis, N.; van de Lagemaat, J., *Coord. Chem. Rev.* **2004**, *248*, 1165-1179.
23. Law, M.; Greene, L. E.; Johnson, J. C.; Saykally, R.; Yang, P., *Nat. Mater.* **2005**, *4*, 455-459.
24. Baxter, J. B.; Walker, A. M.; van Ommering, K.; Aydil, E. S., *Nanotech.* **2006**, *17*, S304-S312.
25. Kamat, P. V., *J. Phys. Chem. C* **2007**, *111*, 2834-2860.
26. Liu, B.; Aydil, E. S., *J. Am. Chem. Soc.* **2009**, *131*, 3985-3990.

27. Kongkanand, A.; Tvrdy, K.; Takechi, K.; Kuno, M.; Kamat, P. V., *J. Am. Chem. Soc.* **2008**, *130*, 4007-4015.
28. Klem, E. J. D.; MacNeil, D. D.; Lavina, L.; Sargent, E. H., *Adv. Mater.* **2008**, *20*, 3433-3439.
29. Luther, J. M.; Law, M.; Beard, M. C.; Song, Q.; Reese, M. O.; Ellingson, R. J.; Nozik, A. J., *Nano Lett.* **2008**, *8*, 3488-3492.
30. Koleilat, G. I.; Levina, L.; Shukla, H.; Myrskog, S. H.; Hinds, S.; Pattantyus-Abraham, A. G.; Sargent, E. H., *ACS Nano* **2008**, *2*, 833-840.
31. Liljeroth, P.; Overgaag, K.; Urbieta, A.; Grandidier, B.; Hickey, S. G.; Vanmaekelbergh, D., *Phys. Rev. Lett.* **2006**, *97*, 096803(4).
32. Talapin, D. V.; Murray, C. B., *Science* **2005**, *310*, 86-89.
33. Law, M.; Luther, J. M.; Song, Q.; Hughes, B. K.; Perkins, C. L.; Nozik, A. J., *J. Am. Chem. Soc.* **2008**, *130*, 5974-5985.
34. Luther, J. M.; Law, M.; Song, Q.; Perkins, C. L.; Beard, M. C.; Nozik, A. J., *ACS Nano* **2008**, *2*, 271-280.
35. Wang, L.-W.; Zunger, A., *Phys. Rev. B* **1996**, *53*, 9579(4).
36. Karazhanov, S. Zh.; Lew Yan Voon, L. C., *Semiconductors* **2005**, *39*, 161-173.
37. Jdira, L., Liljeroth, P.; Stoffels, E.; Vanmaekelbergh, D., Speller, S., *Phys. Rev. B* **2006**, *73*, 115305(6).
38. Meulenberg, R. W.; Lee, J. R. I.; Wolcott, A.; Zhang, J. Z.; Terminello, L. J., van Buuren, T., *ACS Nano* **2009**, *3*, 325-330.

39. Inamdar, S. M.; Ingole, P. P.; Haram, S. K., *ChemPhysChem* **2008**, *9*, 2574-2579.

40. Guyot-Sionnest, P.; Wehrenberg, B.; Yu, D., *J. Chem. Phys.* **2005**, *123*, 074709(7).

41. Kippeny, T. C.; Bowers, M. J.; Dukes, A. D.; McBride, J. R.; Orndorff, R. L.; Garrett, M. D.; Rosenthal, S. J., *J. Chem. Phys.* **2008**, *128*, 084713(7).

42. Wuister, S. F.; de Mello Donegá, C.; Meijerink, A., *J. Phys. Chem. B* **2004**, *108*, 17393-17397.

43. Pokrant, S.; Whaley, K. B., *Eur. Phys. J. D* **1999**, *6*, 255-267.

44. Puzder, A.; Williamson, A. J.; Gygi, F.; Galli, G., *Phys. Rev. Lett.* **2004**, *92*, 217401(4).

45. Alperson, B.; Rubinstein, I.; Hodes, G., *Phys. Rev. B* **2001**, *63*, 081303(4).

46. Bowen Katari, J. E.; Colvin, V. L.; Alivisatos, A. P., *J. Phys. Chem.* **1994**, *98*, 4109-4117.

47. Taylor, J.; Kippeny, T.; Rosenthal, S. J., *J. Cluster Sci.* **2002**, *12*, 571-582.

48. Murray, C. B.; Sun, S.-H., Gaschler, W.; Doyle, H.; Betley, T. A.; Kagan, C. R., *IBM J. Res. & Dev.* **2001**, *45*, 47-56.

49. Schaller, R. D.; Klimov, V. I., *Phys. Rev. Lett.* **2004**, *92*, 186601(4).

50. Wise, F. W., *Acc. Chem. Res.* **2000**, *33*, 773-780.

51. Wehrenberg, B. L.; Guyot-Sionnest, P., *J. Am. Chem. Soc.* **2003**, *125*, 7806-7807.
52. Franceschetti, A., *Phys. Rev. B* **2008**, *78*, 075418(6).
53. Mentzel, T. S.; Porter, V. J.; Geyer, S.; MacLean, K.; Bawendi, M. G.; Kastner, M. A., *Phys. Rev. B* **2008**, *77*, 075316(8).
54. Hummer, K.; Grüneis, A.; Kresse, G., *Phys. Rev. B* **2007**, *75*, 195211(9).
55. Harbold, J. M.; Wise, F. W., *Phys. Rev. B* **2007**, *76*, 125304(6).
56. An, J. M.; Franceschetti, A.; Dudiy, S. V.; Zunger, A., *Nano Lett.* **2006**, *6*, 2728-2735.
57. Kim, D. I.; Islam, M. A.; Avila, L.; Herman, I. P., *J. Phys. Chem. B* **2003**, *107*, 6318-6323.
58. Steiner, D.; Aharoni, A.; Banin, U.; Millo, O., *Nano Lett.* **2006**, *6*, 2201-2205.
59. Liljeroth, P.; Zeijlmans van Emmichoven, P. A.; Hickey, S. G.; Weller, H.; Grandidier, B.; Allan, G.; Vanmaekelbergh, D., *Phys. Rev. Lett.* **2005**, *95*, 086801(4).
60. Williams, K. J.; Tisdale, W. A.; Leschkies, K. S.; Haugstad, G.; Norris, D. J., Aydil, E. S.; Zhu, X.-Y., *ACS Nano* **2009**, *3*, 1532-1538.
61. Allan, G.; Delerue, C., *Phys. Rev. B* **2004**, *70*, 245321(9).
62. Moreels, I.; Lambert, K.; De Muynck, D.; Vanhaecke, F.; Poelman, D.; Martins, J. C.; Allan, G.; Hens, Z., *Chem. Mater.* **2007,** *19,* 6101–6106.
63. Dai, Q.; Wang, Y.-N.; Li, X.; Zhang, Y.; Pellegrino, D. J.; Zhao, M.; Zou, B.; Seo, J.-T.; Wang, Y.; Yu, W. W., *ACS Nano* **2009**, *3*, 1518-1524.

64. Moreels, I.; Fritzinger, B.; Martins, J. C.; Hens, Z., *J. Am. Chem. Soc.* **2008**, *130*, 15081-15086.

Chapter 2. Experimental Methods

2.1 Introduction

This chapter will describe the instrumental methods used in the experiments detailed in Chapters Three and Four, including x-ray photoelectron spectroscopy and ultraviolet photoelectron spectroscopy. An account will be presented of the model interfaces studied, as well as the analysis used in constructing diagrams of interfacial energy alignment.

2.2 X-ray Photoelectron Spectroscopy

Photoelectron or photoemission spectroscopy is a powerful technique for surface analysis that is based on the photoelectric effect. If light incident on a surface is of sufficiently high energy, then electrons will be ejected from the material. Analysis of the spectral and angular distribution of photoejected electrons allows for elemental identification and insight into bonding interactions.

Due to energy conservation the binding energy of an electron can be determined from photoemission as follows:

$$E_b = h\nu - E_k - \varphi_s \qquad (2.2.1)$$

, where E_b is the binding energy, $h\nu$ is the (monochromatic) light energy, E_k is the measured kinetic energy of the electron, and φ_s is a small correction due to the work function of the spectrometer.

X-ray photoelectron spectroscopy (XPS) is so named because of the photon source used for excitation. The binding energies of many core atomic orbitals fall in the range of soft x-rays (1-100 keV); hence, this technique is concerned with characterization of core electronic levels, in contrast to ultraviolet photoelectron spectroscopy, which will be described in the next section. Since photoelectron peaks from atomic orbitals are generally sharp and well resolved in energy, a plot of photoelectron intensity versus binding energy gives an unambiguous determination of elemental composition. Another important concept in XPS is the chemical shift: a difference in oxidation state of an element is felt by its core atomic orbitals and is manifest as a small shift in binding energy. Thus, high resolution scans of a specific photoelectron peak can reveal rich variation in the local bonding environment on the atomic scale.

X-ray photoelectron spectroscopy is inherently surface sensitive due to the mean free path of an electron in a solid, or the average distance an electron will travel between collisions. If a photoexcited electron undergoes inelastic scattering on the way to the sample surface the electronic signature of the orbital that has been vacated is lost. This inelastically scattered electron is then called a secondary electron and contributes to the background signal in photoemission spectroscopy, which increases significantly at low kinetic energies. Thus, the mean free path is also considered as the electron escape depth, or the distance into the surface that can be sampled. The need to avoid inelastic scattering also requires that the experiment be performed in ultrahigh vacuum conditions. The mean free path is a function of electron kinetic energy but rather independent of material composition, having a value less than about 2 nm over all kinetic energies pertinent for photoemission spectroscopy.

X-ray photoelectron spectra are collected using an x-ray anode that produces Mg K_α radiation (E = 1253.6 eV), operated at 200 W. The ultrahigh vacuum chamber is equipped with a Phi 5400 concentric hemispherical analyzer. Analyzer pass energies of 89.5 eV and 17.9 eV are used for collection of survey and high resolution scans, respectively. The sample normal direction is positioned at 45˚ to the detector, and all measurements are taken at 300 K.

2.3 Ultraviolet Photoelectron Spectroscopy

Ultraviolet photoelectron spectroscopy (UPS) is a technique for probing the energetic structure of valence electronic levels. In contrast to XPS this method cannot be used for elemental identification because all materials have valence electrons within several eV of the Fermi level. These high energy states participate in bonding interactions and electrical conduction, and they are generally broad, occurring as bands of allowed energies rather than discrete levels.

The UP spectrum is a direct measure of the density of occupied states. Figure 2-1 illustrates the concept of UPS. The occupation of states below the Fermi level is designated by shading. Monochromatic light impinges on the sample and promotes all occupied levels by the same energy, reproducing the intensity distribution (density of states) in the vacuum. Clearly, there is an

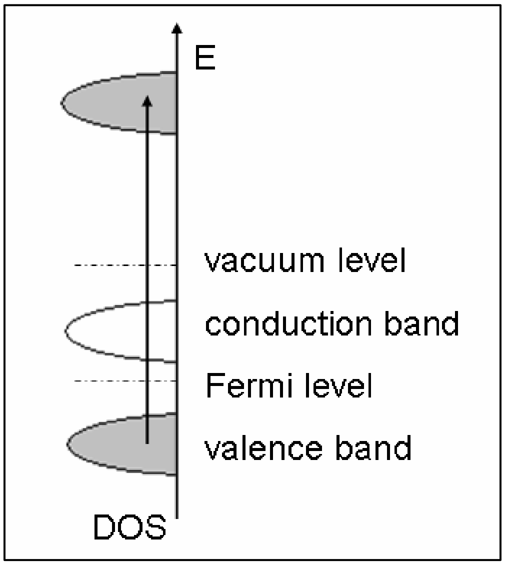

Figure 2-1. Schematic description of ultraviolet photoemission spectroscopy.

DOS = density of states. Shading represents occupation of the valence band.

energy limit to the technique in that no states with a binding energy higher than the photon energy can escape the sample. In fact, the limit is more severe than this due to the work function of the surface. The work function is the energy required for an electron to overcome the attractive potential of the surface and break away into the vacuum; in practice, it is the energy difference between the vacuum and Fermi levels. The value of the surface work function can be easily determined from UPS measurements by the energy cutoff at the low kinetic energy end of the spectrum. The measured work function depends on many factors, including surface roughness, surface dipoles, and the presence of adsorbates.

To make a strict comparison between UPS data and a calculated density of states (DOS) distribution, one would need to subtract the background due to secondary electrons and integrate the spectrum over all emission angles. In principle the band structure of a single crystal can be experimentally measured using angle-resolved measurements. Since crystal momentum is conserved in the plane parallel to the surface, the angle of photoemission is related to the parallel momentum through the following relation:

$$\hbar k_{II} = \sqrt{2m_e E_K} \cdot \sin\theta \qquad (2.3.1)$$

, where k_{II} is the magnitude of the parallel momentum vector, m_e is the rest mass of an electron, E_k is the measured kinetic energy of the photoelectron, and θ is the angle between the surface normal direction and the detector. Films of quantum dots, however, lack the translational symmetry required to justify the relation in Equation 2.3.1, so angle-resolved photoemission measurements are of questionable utility and have not been reported in the literature for quantum dots. Also, variation of the angle of photoelectron detection can adjust the sampled depth via the expression

$$z = \lambda \cos\theta \qquad (2.3.2)$$

, where z is the effective sampling depth, λ is the mean free path as described in the previous section, and θ is the same as that in Eq. 2.3.1. Thus, grazing angle detection geometry can enhance surface sensitivity. This variation of effective sampling depth can be useful for determining the spectral location of contributions from surface contaminants. For all samples that are prepared in or exposed to the ambient environment the adsorption of adventitious hydrocarbon species, water or oxygen molecules on the surface can be problematic for quantification purposes. Adsorbates can attenuate the signal of interest, due to the very short mean free path of the electron discussed above, and lead to broadening of otherwise sharp features. All of the UP spectra presented in Chapters Three and Four were collected in normal emission geometry to maximize probing depth. Measurements were also collected as a function of emission angle. The relative intensities of spectral features were found to change with detection angle but never the peak positions, indicative of a variation in sampling depth and not momentum dispersion. The features due to surface contaminant species, accentuated in grazing angle detection, are found several eV below the valence band edge of the quantum dots and do not preclude the measurement of interfacial alignment.

All UP spectra are collected using He-I radiation (E = 21.2 eV), produced in a differentially pumped rare gas discharge lamp that is operated at 25 W. The light is collimated in a quartz capillary, resulting in an irradiated spot size on the sample of around 1 mm^2. The light is incident at 50° from the sample normal direction. All photoelectrons are detected along the sample normal direction, as mentioned above, with an analyzer pass energy of 4.45 eV. The samples are biased at -8.0 V in order to resolve the secondary electron threshold of the sample. The energy scale is referenced to the Fermi level.

2.4 Preparation of Model Interfaces

In order to directly study interfacial energy alignment in quantum dot-sensitized solar cells by photoemission spectroscopy model quantum dot-oxide interfaces have been prepared using single crystal transition metal oxides as substrates. Single crystals have well known photoemission spectra and provide a structurally defined and flat platform for interface formation. One side-polished ZnO $(10\bar{1}0)$ and two side-polished rutile TiO_2 (110) wafers were purchased from MTI Corporation, and their surface preparation will be described below. As-received TiO_2 crystals were too resistive for photoemission measurements, and were therefore subject to the following treatment: annealing at 1000 K *in vacuo* to produce bulk oxygen vacancies and *n*-type conductivity, with subsequent sputtering by 1000 eV Ar^+ and surface re-oxidation via annealing in low pressure (~ 1 x 10^{-7} Torr) O_2 atmosphere.[1] These particular crystal facets were selected as they have the lowest surface energy for their respective material and are therefore expected to be well represented on nanoparticle surfaces. For instance, it is known that the $(10\bar{1}0)$ and related planes comprise the (long) sides of crystalline ZnO nanowires.[2] The following sections will describe the preparation of the samples that are examined in Chapters Three and Four.

2.4.1 Cadmium Selenide on Zinc Oxide

The method used to prepare the CdSe quantum dots on the single crystal ZnO surface was the same as that used in making the nanowire based quantum dot-sensitized solar cell described by Leschkies *et alia*.[3] Luminescent CdSe quantum dots were prepared from a CdO precursor according to standard methods.[4] Particle sizes were controlled by varying the reflux time of the precursor solutions. Post-synthesis size distributions were narrowed by size-selective precipitation. Standard deviation in the diameter of quantum dot ensembles was determined to be ±10% from the full-width-at-half-maximum of the photoluminescence peak. Mean particle sizes were obtained by measuring UV/vis absorption spectra. The lowest energy exciton absorption peak positions of the four batches of particles were λ = 468, 488, 530, and 592 nm, corresponding to particle diameters of D = 2.1, 2.2, 2.7, and 4.2 nm, respectively, as determined from the published calibration curve of Yu *et alia*.[5]

The as-synthesized quantum dots were capped by tri-*n*-octylphosphine oxide (TOPO). In order to facilitate assembly of CdSe quantum dots on the ZnO surface, 3-mercaptopropionic acid (MPA) linkers were introduced via a ligand exchange reaction as described previously;[6] precipitated TOPO-CdSe dots were dispersed in 20 mM MPA solutions in methanol and refluxed 6-24 h under N_2 atmosphere. The resulting CdSe quantum dots were passivated by the MPA ligands through thiolate bonds to Cd^{2+} sites. The basic conditions (pH > 11, by addition of tetramethylammonium hydroxide) of the ligand exchange solution leave the carboxyl groups on the outer shell of the MPA monolayer deprotonated, as evidenced by FTIR measurements.[3] MPA-CdSe particles were purified by a series of precipitation-centrifugation cycles. After the third centrifugation cycle, the MPA-capped CdSe quantum dots were dispersed in aqueous solution (NaOH, pH ~ 11) and titrated to slightly basic pH (< 7.5) by adding 10 mM HCl dropwise while stirring. The solutions maintained clarity throughout all sample preparation, indicating the stable dispersion of the MPA-capped quantum dots.

One-side polished ZnO wafers of $(10\bar{1}0)$ orientation were purchased from MTI Corporation. To prepare a composite sample (i.e., ZnO with MPA-CdSe quantum dots), a freshly etched (5 minutes in 1 mM HNO_3) ZnO substrate was placed into a freshly titrated quantum dot dispersion. The coverage of the MPA-CdSe quantum dots on the ZnO surface was adjusted by ZnO incubation time (minutes to days) in the quantum dot dispersion. Upon removal from the quantum dot dispersion, the composite sample was rinsed thoroughly with deionized water, blown dry with nitrogen gas, and quickly transferred to the load-lock of the ultrahigh vacuum chamber for measurements.

2.4.2 Lead Selenide on Zinc Oxide and Titanium Dioxide

All PbSe quantum dot preparation and processing steps were carried out under inert atmosphere in a glove box. PbSe quantum dots capped with oleic acid were prepared from a PbO precursor according to standard methods.[7, 8] Particle sizes were controlled by varying the reflux time of the precursor solutions. Post-synthesis size distributions were narrowed by size-selective precipitation. Standard deviation in the diameter of quantum dot ensembles was determined to be ±5% from the full-width-at-half-maximum of the first excitonic absorption peak. Mean particle sizes were obtained by measuring UV/vis absorption spectra. The lowest energy exciton absorption peak positions of the two batches of particles were λ = 1108 and 2015 nm, corresponding to particle diameters of D = 3.4 and 6.7 nm, respectively, as determined from the published calibration curve of Dai *et alia*.[9]

Clean ZnO crystals were etched 5 minutes in 1 mM HNO_3, and clean TiO_2 crystals were etched 30-60 minutes in 1 M HCl while under UV ($h\nu$ = 254 nm) illumination, following the preparation by Lu *et al*.,[10] immediately before transfer to the glove box. Nanoparticle films were prepared by dip coating in colloidal dispersions in hexanes and withdrawn from the dispersion at a rate of 1 cm/s. Dispersion concentrations were 1 mg/mL unless otherwise noted. This concentration was chosen to give sub-monolayer coverage on the substrate. Quantum dot coverage in these experiments was not quantified except by comparison to atomic force microscope images taken in our lab for identically prepared samples.[11] Hydrazine (N_2H_4) treated samples were submerged in a 1 M hydrazine solution in acetonitrile for 30-60 minutes, while 1,2-ethanedithiol (EDT) treated samples were submerged in 0.1 M EDT solutions in acetonitrile for 1-40 minutes. The ligand treatment durations were selected such that oleate removal from the sub-monolayer film was complete as determined by FTIR measurements. All ligand-treated quantum dot films were rinsed with acetonitrile to remove weakly adsorbed species and mounted on sample holders before being removed from the glove box. During the transfer to the ultrahigh vacuum chamber, samples were exposed to air for < 10 s; however, no noticeable oxidation of either Pb or Se was observed in XPS measurements performed on identically prepared samples.

2.5 Construction of Alignment Diagrams

Photoemission spectroscopy has been used extensively to characterize band offsets between two materials. It provides a direct measure of density of states on a common, absolute energy scale. However, interpretation of measured energy levels must be performed with care.

In theory there are two regimes of interfacial energy alignment: vacuum level alignment and Fermi level pinning. Vacuum level alignment generally occurs at heterojunctions for which no interfacial charge redistribution (i.e. equilibration of chemical potentials) can occur. For instance, vacuum level alignment has been observed at various metal-organic interfaces in which the highest occupied molecular orbital (HOMO) of the organic material is located more than about 0.5 eV below the Fermi level of the metal.[12] This was reasoned to be too large a barrier for charge transfer. Figure 2-2 depicts vacuum level alignment at an organic-metal interface. The vacuum level, E_{vac}, is aligned (i.e. shows no discontinuity) across the interface. Of course, the vacuum level *at the interface* is only a hypothetical concept; the two materials are actually in contact. In general the ionization potential (IP) of the organic and the work function of the metal (Φ_{metal}) are known, from electrochemical or photoemission measurements, before the junction is formed. Φ_{film} is called the "effective" work function of the film because it has been observed that the position of E_f within the band gap of an organic semiconductor often depends on the metal substrate used for deposition and is, therefore, not an intrinsic property of the organic material.[13] It is interesting to note that vacuum level alignment is often assumed in predicting favorable donor/acceptor material combinations for devices, yet it is not the general rule.

In contrast, Fermi level pinning has been found to occur at interfaces where the Fermi level of the substrate is very near to a band edge (VBM/CBM or HOMO/LUMO) of the overlayer. Fermi level pinning is often assumed to be related to the presence of a peak in the distribution of defect states, which in this context are called charge transfer states.[12] The Fermi level becomes

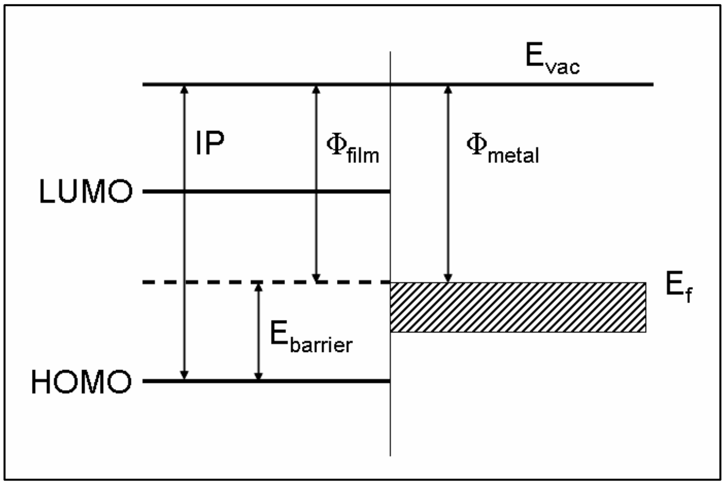

Figure 2-2. Schematic description of vacuum level alignment between an organic semiconductor and a metal. E_{vac} is the vacuum level; IP is the ionization potential of the organic semiconductor; Φ_{film} is the effective work function of the organic film; Φ_{metal} is the work function of the metal substrate; LUMO and HOMO levels refer to the lowest unoccupied and highest occupied molecular orbital, respectively, of the organic material; E_f is the Fermi level; and $E_{barrier}$ is the barrier to charge transfer between the two materials. Scheme adapted from Braun *et alia*.[12]

pinned at the position of the charge transfer states (see Figure 2-3). The occurrence of Fermi level pinning is deduced through a series of measurements in which the energy level of one material is varied systematically, say by using different metal substrates with different work functions. Once the Fermi level is pinned, any further change in substrate work function will be manifest as a vacuum level offset (Δ). In general there are many contributions to an observed vacuum level offset, including interfacial dipoles, chemical bonding or charge redistribution, band bending in the substrate, or surface dipoles, and it is difficult to separate all the contributions.

In the experiments detailed in Chapters Three and Four it is assumed that the Fermi level is aligned between the substrate and the quantum dots. Control experiments verified that the substrate is in equilibrium with the spectrometer; i.e. depositing metal Ohmic contacts on the back side of the substrate wafers did not result in any spectral shifts. Sample charging did not occur, as evidenced by equal spectral intensity from samples with and without quantum dots, as well as the small (≤ 0.4 eV) shift in vacuum level across all samples. In addition, very low quantum dot coverages were used throughout, which both increases the probability that electrical equilibration occurs between the materials and allows a more direct study of interface-specific properties. Finally, the substrates were observed to have large densities of surface states, extending in effect from the valence band edge all the way to the Fermi level, and therefore there are multitudinous opportunities for charge transfer with the quantum dots. This assumption of Fermi level equilibration is especially

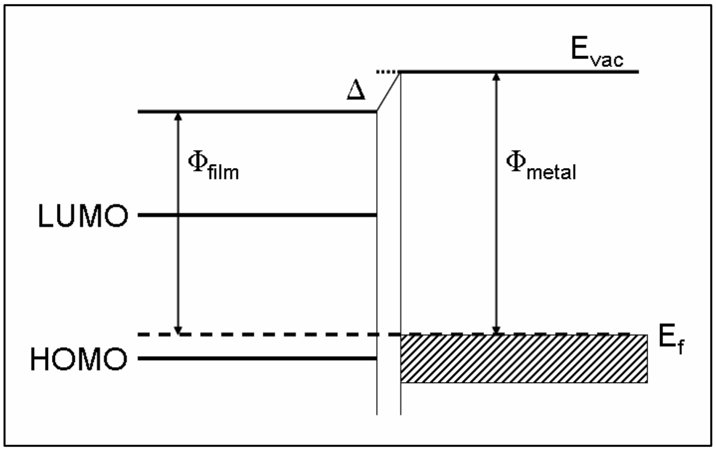

Figure 2-3. Schematic description of Fermi level pinning between an organic semiconductor and a metal. E_{vac} is the vacuum level; Δ is the vacuum level offset at the interface; Φ_{film} is the effective work function of the organic film; Φ_{metal} is the work function of the metal substrate; LUMO and HOMO levels refer to the lowest unoccupied and highest occupied molecular orbital, respectively, of the organic material; and E_f is the Fermi level. Scheme adapted from Braun *et alia*.[12]

important in regard to the PbSe samples described in Chapter Four, since spectral features due to the substrates were not observed after quantum dot deposition.

Surface states from the quantum dots were not observed in these experiments. This could be due to the low coverage of nanoparticles on the surface. The CdSe samples were extensively exposed to aqueous solutions, and it might be expected that any surface states would then be passivated by adsorbed water molecules.[14] Though the PbSe samples were only exposed to air for less than 10 seconds in transfer to the ultrahigh vacuum chamber, water adsorption onto the particle surface cannot be ruled out. The positions of quantum dot surface states with respect to the band edges are not generally known. In fact, the position of the Fermi level within the particle band gap is not known *a priori*, though it is often assumed to be in the middle of the gap. It is expected that the exact position of the Fermi level will depend strongly on details of the quantum dot surface. In any case, there is not enough experimental evidence to make conclusions about the influence of quantum dot surface states on interfacial energy alignment in the present measurements.

Finally, optical absorbance measurements are used to infer the alignment of the excited (conduction) states. Thus, the quantum dot LUMO level is stabilized by the exciton binding energy, which is less than 0.2 eV for the size range of CdSe nanoparticles studied here [15] and expected to be very small in PbSe.[16] However, since excitons are directly produced upon photoexcitation in quantum dots, these Coulomb-stabilized levels are relevant to charge injection in actual devices. Though, it is important to remember that low-lying excited states are not the only levels available for interfacial charge transfer; injection of hot electrons is currently being considered as a method for further improving device efficiency.

2.6 References

1. Onda, K.; Li, B.; Petek, H., *Phys. Rev. B* **2004**, *70*, 045415(11).
2. Diebold, U.; Koplitz, L. V.; Dulub, O., *Appl. Surf. Sci.* **2004**, *237*, 336-342.
3. Leschkies, K. S.; Divakar, R.; Basu, J.; Enache-Pommer, E.; Boercker, J. E.; Carter, C. B.; Kortshagen, U. R.; Norris, D. J.; Aydil, E. S., *Nano Lett.* **2007**, *7*, 1793-1798.
4. Reiss, P.; Bleuse, J.; Pron, A., *Nano Lett.* **2002**, *2*, 781-784.
5. Yu, W. W.; Qu, L.-H.; Guo, W.-Z.; Peng, X.-G., *Chem. Mater.* **2003**, *15*, 2854-2860.
6. Aldana, J.; Wang, Y. A.; Peng, X.-G., *J. Am. Chem. Soc.* **2001**, *123*, 8844-8850.
7. Murphy, J. E.; Beard, M. C.; Nozik, A. J., *J. Phys. Chem. B* **2006**, *110*, 25455-25461.
8. Luther, J. M.; Law, M.; Song, Q.; Perkins, C. L.; Beard, M. C.; Nozik, A. J., *ACS Nano* **2008**, *2*, 271-280.
9. Dai, Q.; Wang, Y.-N.; Li, X.; Zhang, Y.; Pellegrino, D. J.; Zhao, M.; Zou, B.; Seo, J.-T.; Wang, Y.; Yu, W. W., *ACS Nano* **2009**, *3*, 1518-1524.
10. Lu, Y.-F.; Jaeckel, B.; Parkinson, B. A., *Langmuir* **2006**, *22*, 4472-4475.
11. Williams, K. J.; Tisdale, W. A.; Leschkies, K. S.; Haugstad, G.; Norris, D. J., Aydil, E. S.; Zhu, X.-Y., *ACS Nano* **2009**, *3*, 1532-1538.
12. Braun, S.; Osikowicz, W.; Wang, Y.; Salaneck, W. R., *Organic Electronics* **2007**, *8*, 14-20.

13. Tang, J. X.; Lee, C. S.; Lee, S. T., *J. Appl. Phys.* **2007**, *101*, 064504(4).

14. Alperson, B.; Rubinstein, I.; Hodes, G., *Phys. Rev. B* **2001**, *63*, 081303(4).

15. Meulenberg, R. W.; Lee, J. R. I.; Wolcott, A.; Zhang, J. Z.; Terminello, L. J., van Buuren, T., *ACS Nano* **2009**, *3*, 325-330.

16. Kang, I.; Wise, F. W., *J. Opt. Soc. Am. B* **1997**, *14*, 1632-1646.

Chapter 3. Valence Band Alignment at Cadmium Selenide Quantum Dot and Zinc Oxide Interfaces

Reproduced in part with permission from

J. Phys. Chem. C 2008, 112, 8419-8423

3.1 Introduction

Excitonic solar cells have become a major focus in solar energy research.[1] In the best known example, the dye-sensitized solar cell,[2] excitons are photogenerated in a dye molecule adsorbed on TiO_2 nanocrystals and dissociate rapidly to inject electrons in the TiO_2 conduction band; the positively charged dye is reduced through an electrochemical reaction with a redox couple in an electrolyte that penetrates the mesoporous space between the TiO_2 nanocrystals. The high interfacial surface area of the TiO_2 nanocrystals allows for efficient light absorption and exciton dissociation. In the quest for higher light-to-electric power conversion efficiency and lower production cost, a number of researchers have proposed the quantum dot-sensitized solar cell architecture where nanoparticles or nanowires of wide band gap semiconductors such as ZnO or TiO_2 are photosensitized with quantum dots of III-V or II-VI semiconductors.[3-10] In these types of cells, excitons are photogenerated in the quantum dots and dissociate to inject electrons into the wide band gap semiconductor. The hole left behind in the quantum dot is reduced by the electrolyte as in the dye-sensitized solar cell. The crystalline nanowires are presumed to provide an efficient and direct pathway to the electrode for photoinjected electrons by way of extended conduction band states. The motivation for introducing quantum dots is several-fold: firstly, one can exploit quantum confinement effects to optimize overlap of the absorption spectrum with the solar spectrum; secondly, inorganic semiconductor quantum dots are expected to exhibit enhanced stability with respect to photobleaching as compared to organometallic dyes; and finally, the recently discovered phenomenon of multiple exciton generation in inorganic quantum dots allows for the possibility of increased quantum efficiencies in light-to-electric current conversion.[11, 12]

A key issue governing efficient electron transfer between two semiconductors (and, consequently, photocurrent generation) is interfacial energy alignment. In a dye- or quantum dot-sensitized solar cell, the energy level of the transient electron (e.g. the lowest unoccupied molecular orbital) within the exciton must lie above the conduction band minimum (CBM) of the wide band gap semiconductor (e.g. TiO_2 or ZnO) while that of the hole must lie below the valence state of the hole conductor (e.g. the electrochemical potential of the redox couple in the electrolyte). An optimal alignment of electronic energy levels at the interface is a balance between multiple factors. On the one hand, the rate of electron transfer is a function of the density of states in the acceptor. Within the parabolic band approximation, the density of states at the conduction band minimum is zero and increases as $\sqrt{(E - CBM)}$. Thus, the excited donor levels must lie sufficiently above the CBM where the density of states is high enough to make electron injection into the semiconductor competitive with other relaxation processes. On the other hand, excess energy (i.e. the amount that is over and above the CBM) of the photoinjected electron can be rapidly thermalized by electron-phonon scattering and not recovered as electrical energy. So, the ability to tune electronic energy alignment at the quantum dot-semiconductor interface allows one to optimize solar-to-electric power conversion efficiencies in semiconductor quantum dot-based excitonic solar cells.

Interfacial electronic energy alignment has been investigated in a model system, where colloidal CdSe quantum dots are assembled on a single crystal ZnO ($10\bar{1}0$) substrate via molecular linkers. ZnO has a band gap (3.4 eV) and an electron affinity (4.2 eV) similar to those of TiO_2; it is explored as a viable alternative to TiO_2 in dye- and quantum dot-sensitized solar cells. A particularly attractive property of ZnO is the ease with which crystalline nanowires can be grown. Indeed, several groups have reported dye- or quantum dot-sensitized solar cells as well as bulk heterojunction type solar cells based on ZnO nanowire arrays.[3, 4, 8, 13] ZnO nanowires grow along the *c*-axis, a consequence of the anisotropic wurtzite unit cell. The side facets of these nanowires have ($10\bar{1}0$) or equivalent orientations.[14] Thus, exciton dissociation in these ZnO nanowire solar cells occurs preferentially on the ($10\bar{1}0$) or equivalent surfaces. Also, CdSe is chosen because it is among the most extensively studied quantum dot systems and has been recently demonstrated as the light absorber in ZnO nanowire-based solar cells.[8] The optical gap in CdSe quantum dots is broadly tunable in the visible region by particle size. This allows tuning of the interfacial electronic energy alignment by varying the size of the quantum dots. The surfaces of CdSe quantum dots are passivated with a short molecular linker, 3-mercaptopropionic acid (MPA), and assembled onto the ZnO surface via carboxylate linkages. Ultraviolet photoelectron spectroscopy (UPS) is used to determine the alignment of the valence band maximum (VBM) of the CdSe quantum dots to the VBM of ZnO. Together with the optical gap of the quantum dots and the known band gap of ZnO, the alignment of the CBM levels of CdSe quantum dots and ZnO is derived. In analogy to molecules, the VBM and CBM of the quantum dots are also referred to as the highest occupied molecular orbital (HOMO) and lowest unoccupied molecular orbital (LUMO) levels.

Photoemission spectroscopy has been applied before to the characterization of valence electronic structure of nanoparticles and other nanostructures. Colvin *et al.* carried out UPS measurements of CdS quantum dots on self-assembled monolayer covered metal structures and showed a downward shift of the valence band edge by as much as 0.63 eV as quantum dot size decreased.[15] Similar results were reported by Wu *et al*., who also pointed out the importance of final state effects due to the insulating nature of the organic passivation layers.[16] Based on x-ray absorption spectroscopy, Lee *et al.* reported that the conduction band states in CdSe quantum dots increased by as much as 1 eV as their size decreased.[17] However, none of these previous studies addressed the alignment issue at the quantum dot-substrate interface.

3.2 Experimental

The method used to prepare the CdSe quantum dots on the single crystal ZnO surface was the same as that used in making the nanowire based quantum dot-sensitized solar cell described in Ref. [8]. Luminescent CdSe quantum dots were prepared from a CdO precursor according to standard methods.[18] Particle sizes were controlled by varying the reflux time of the precursor solutions. Post-synthesis size distributions were narrowed by size-selective precipitation. Standard deviation in the diameter of quantum dot ensembles was determined to be ±10% from the full-width-at-half-maximum of the photoluminescence peak. Mean particle sizes were obtained by measuring UV/vis absorption spectra. The lowest energy exciton absorption peak positions of the four batches of particles were λ = 468, 488, 530, and 592 nm, corresponding to particle diameters of D = 2.1, 2.2, 2.7, and 4.2 nm, respectively, as determined from the published calibration curve of Yu *et alia*.[19]

The as-synthesized quantum dots were capped by tri-*n*-octylphosphine oxide (TOPO). In order to facilitate assembly of CdSe quantum dots on the ZnO surface, 3-mercaptopropionic acid (MPA) linkers were introduced via a ligand exchange reaction as described previously;[20] precipitated TOPO-CdSe dots were dispersed in 20 mM MPA solutions in methanol and refluxed 6-24 h under N_2 atmosphere. The resulting CdSe quantum dots were passivated by the MPA ligands through thiolate bonds to Cd^{2+} sites. The basic conditions (pH > 11, by addition of tetramethylammonium hydroxide) of the ligand exchange solution leave the carboxyl groups on the outer shell of the MPA monolayer deprotonated, as evidenced by FTIR measurements.[8] MPA-CdSe particles were purified by a series of precipitation-centrifugation cycles. After the third centrifugation cycle, the MPA-capped CdSe quantum dots were dispersed in aqueous solution (NaOH, pH ~ 11) and titrated to slightly basic pH (< 7.5) by adding 10 mM HCl dropwise while stirring. The solutions maintained clarity throughout all sample preparation, indicating the stable dispersion of the MPA-capped quantum dots.

To prepare a composite sample (i.e., ZnO with MPA-CdSe quantum dots), a freshly etched (5 minutes in 1 mM HNO_3) ZnO substrate was placed into a freshly titrated quantum dot dispersion. The coverage of the MPA-CdSe quantum dots on the ZnO surface was adjusted by ZnO incubation time (minutes to days) in the quantum dot dispersion. Upon removal from the quantum dot dispersion, the composite sample was rinsed thoroughly with deionized water, blown dry with nitrogen gas, and quickly transferred to the load-lock of the ultrahigh vacuum chamber for measurements.

Electronic band alignment was determined by ultraviolet photoelectron spectroscopy (UPS) and CdSe quantum dot coverage on the ZnO $(10\bar{1}0)$ surface by x-ray photoelectron spectroscopy (XPS). All spectra were collected at room temperature in an ultrahigh vacuum photoelectron spectrometer equipped with a hemispherical electron energy analyzer (Phi 5400), with He-I radiation ($h\nu$ = 21.2 eV) as UV source and a Mg K_α ($h\nu$ = 1253.6 eV) anode operated at 200 W as x-ray source. In UPS measurements, the incident UV light was 50˚ from the sample normal, and photoelectrons were collected along the sample normal direction with an analyzer pass energy of 4.45 eV and a sample bias of -6.0 V. The He lamp power was set at 25 W in all UP spectra presented here. In XPS measurements, the x-ray incident angle was 5˚ from the surface normal, and photoelectrons were collected at 55˚ from the sample normal. Analyzer pass energies of 89.45 and 17.9 eV were used for survey scans and high resolution scans, respectively. The uncertainty in the measured binding energy is ± 0.1 eV.

3.3 Results and Discussion

Figure 3-1 compares UP spectra of the clean ZnO $(10\bar{1}0)$ surface with those obtained from ZnO surfaces covered with a sub-monolayer of MPA-capped CdSe quantum dots (D = 2.7 nm) at 6% and 12% coverages. The binding energy scale is referenced to the Fermi level. The trace of bare ZnO $(10\bar{1}0)$ (solid) is characterized by two main features in this binding energy region: a distinctive peak (A) at 11 eV originating from Zn 3d core level emission and a broad peak (B) between 4 and 8 eV due to valence band emission with contributions from Zn 4s and O 2p.[21] Point C indicates the valence band edge of ZnO, which will be discussed in detail below. As the surface coverage of CdSe quantum dots is increased (dashed and dotted spectra), features due to ZnO (A and B) are attenuated as expected from the

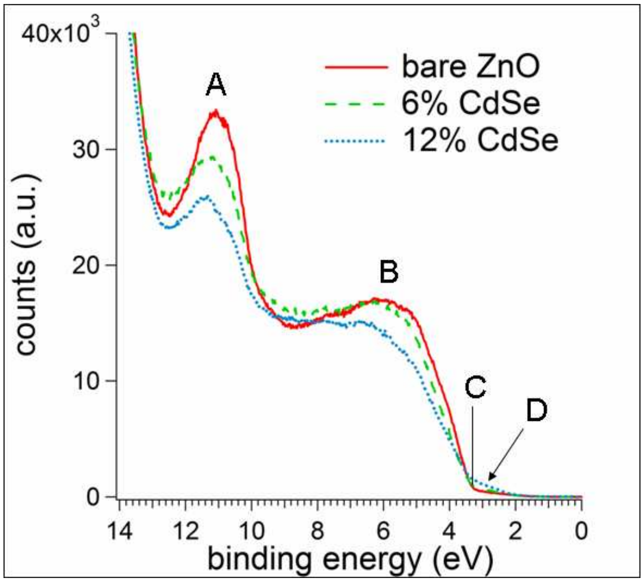

Figure 3-1. UP spectra for MPA-CdSe quantum dots (D = 2.7 nm) on ZnO $(10\bar{1}0)$ as a function of coverage. E = 0 eV on the binding energy scale corresponds to E_f. Background due to secondary electron emission has not been subtracted. See text for assignments of features A, B, C, and D.

presence of the quantum dot adlayer on the ZnO surface. In addition, there is increasing intensity above the ZnO VBM (D); this increased density of states above the VBM correlates with the increase in CdSe coverage and is attributed to photoemission from the valence band of CdSe quantum dots.

A few comments are in order about the coverage calculations employed here. Since both semiconductor valence band edges must be detectable in the UP spectrum for a direct determination of alignment, sub-monolayer coverages of quantum dots are required. The escape depth of photoelectrons in the kinetic energy range accessed by this experiment is 1-2 nm. Thus, a monolayer of MPA-capped CdSe quantum dots—even the smallest used in this study (D = 2.1 nm)—would completely attenuate emission from the ZnO substrate. XPS measurements of the heterogeneous sample surface, containing both MPA-CdSe quantum dots and regions of bare ZnO, do not permit use of typical film-thickness calculations. Therefore, coverage is quantified in these experiments using the atomic ratio of Cd/Zn obtained from the integrated intensity of the Cd $3d_{5/2}$ and Zn $2p_{3/2}$ core emission peaks, corrected with the known atomic sensitivity factors.[22] For example, the coverage of 12% CdSe corresponds to an atomic ratio of Cd/Zn = 0.12.

To obtain valence band alignment at the CdSe-MPA-ZnO interface the region of UP spectra is expanded near the valence band maximum. This region is shown in Figure 3-2 for three different CdSe quantum dot sizes (D = 2.2, 2.7, 4.2 nm), each panel displaying two different coverages. The spectra from quantum dots with D = 2.1 nm (not shown) are nearly identical to those of D =

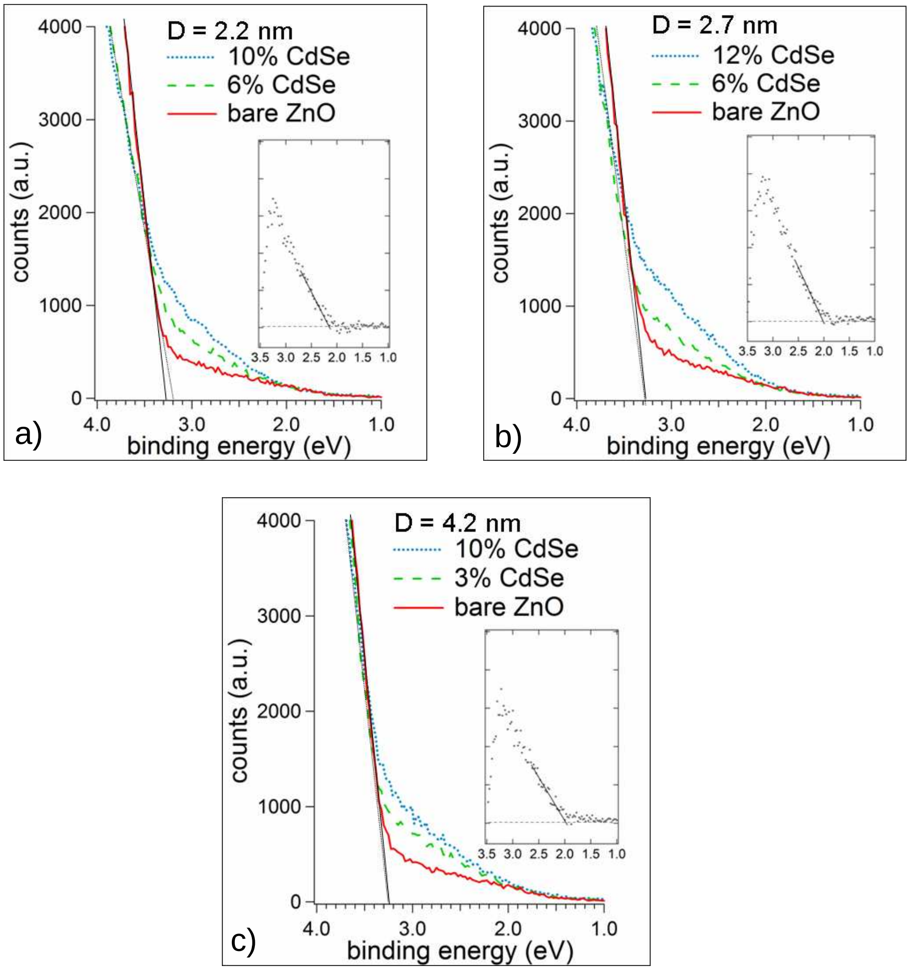

Figure 3-2. Valence region of UP spectra for three sets of MPA-CdSe quantum dots on ZnO $(10\bar{1}0)$ for quantum dot diameters of D = 2.2 (a), 2.7 (b), and 4.2 nm (c). Each panel consists of spectra from clean ZnO $(10\bar{1}0)$ and the ZnO surface adsorbed with MPA-CdSe at two different coverages. Thin gray lines demonstrate the extrapolation to obtain the VBM of ZnO from clean (solid) and quantum dot adsorbed (dashed) surfaces. The inset in each panel shows a difference spectrum between a quantum dot adsorbed and a clean ZnO $(10\bar{1}0)$ surface. The solid line in each inset shows the extrapolation to obtain the VBM of CdSe quantum dots.

2.2 nm, as expected for the closeness in sizes, and are indicative of the excellent reproducibility of the spectra. The VBM of the ZnO substrate is found by linear extrapolation (solid gray and dashed gray lines for clean and CdSe-adsorbed surfaces, respectively) of the leading edge to zero intensity. Using this method, the binding energies for the VBM of clean and quantum dot-adsorbed ZnO ($10\bar{1}0$) were determined to be 3.3 eV and 3.2 eV, respectively. These binding energies are in agreement with reported values for sputtered and annealed ZnO ($10\bar{1}0$) surfaces.[23] Since the band gap of ZnO is 3.4 eV, this places the CBM about 0.2 eV above the Fermi level, consistent with *n*-type behavior. Above the VBM of bare ZnO ($10\bar{1}0$), measurable photoelectron intensity is clearly observed, decaying exponentially into the energy gap. This photoemission is attributed to surface defects within the band gap of ZnO.

With increasing CdSe quantum dot coverage there is an increase in the density of states above the VBM of ZnO, and this is attributed to the CdSe valence band. To accurately obtain the VBM of CdSe quantum dots, a difference spectrum is computed between a CdSe/ZnO composite surface and bare ZnO ($10\bar{1}0$). Difference spectra are shown in the insets of each panel in Figure 3-2. From the difference spectra the VBM of CdSe quantum dots is obtained using linear extrapolation (solid line). This analysis gives a VBM of CdSe at a binding energy of 2.0 eV for quantum dots with D = 2.7 and 4.2 nm and a binding energy of 2.1 eV for quantum dots with D = 2.1 and 2.2 nm. Within experimental uncertainty, these numbers are nearly the same.

It is important to discuss the offsets measured for the vacuum level at the CdSe quantum dot-ZnO ($10\bar{1}0$) interface. For all dot sizes presented here there is a positive vacuum level shift of 0.3 eV; that is, the work function is found to increase from 3.8 eV for the bare substrate to 4.1 eV for MPA-CdSe-adsorbed surfaces. In contrast, the contribution of substrate band bending to the vacuum level offset is found to be slightly size-dependent, with 4.2 and 2.7 nm CdSe quantum dot samples showing bending of 0.1 V and 2.2 nm quantum dot samples showing no substrate band bending. It is reasonable to expect less band bending for the samples with the smallest dots since their valence band has slightly more overlap with that of ZnO, as noted above. And though in principle there may be additional contributions to vacuum level shifts from chemical bond formation or charge redistribution, the offset that remains after correcting for band bending can as a first approximation be attributed to the presence of an interfacial dipole.

Figure 3-3 summarizes the energetic alignment of CdSe quantum dots assembled on the ZnO ($10\bar{1}0$) surface via MPA linkers. The VBM or HOMO positions are determined from UPS measurements as presented above. The exciton levels corresponding to the optical gap were obtained from UV/vis absorbance spectra and are shown as dashed lines. The CBM or LUMO positions of the CdSe quantum dots are obtained from the sum of the HOMO, optical gap, and exciton binding energy. The size-dependent exciton binding energy (E_{ex}) is estimated from the scaling law of Franceschetti and Zunger based on electronic structural calculations.[24] The estimated interfacial dipoles

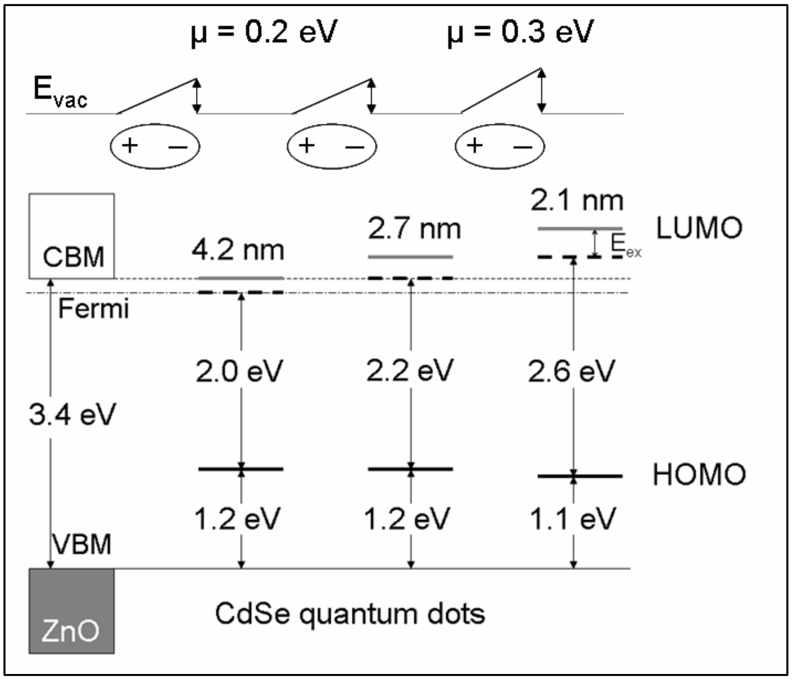

Figure 3.3. Summary energy diagram showing the alignment of the valence band maximum (HOMO) of CdSe quantum dots to the ZnO valence and conduction bands. The HOMO and LUMO energies correspond to transport levels, with the former determined by UPS. The LUMO's were inferred from HOMO + optical band gap + calculated exciton binding energies (E_{ex}). The optical gaps and excitonic levels (thick dashed lines) are shown. The displayed interfacial dipoles (μ) occur at the CdSe quantum dot-ZnO interface.

are displayed as vacuum level offsets, with values of 0.2 eV for 4.2 and 2.7 nm quantum dots and 0.3 eV for 2.2 nm dots. In this simple one-dimensional energy landscape the interfacial dipoles are oriented such that they would act to make electron injection into ZnO more favorable, which may explain the observance of moderately high photocurrent from quantum dot-sensitized solar cells based on these interfaces,[8] even though the energy diagram presented in Fig. 3-3 suggests a poor alignment of the lowest excitonic level with the CBM of ZnO for the larger two dot sizes studied here.

It is concluded from the energy level diagram in Fig. 3-3 that, with decreasing quantum dot size from D = 4.2 to 2.1 nm, the magnitude of the downward shift of the HOMO level is small (≤ 0.1 eV). Within experimental uncertainty, it is at least five times smaller than the upward shift of the LUMO (CBM). In the simplest model of quantum confinement,[25] the VBM and CBM shifts are inversely proportional to the effective mass of the holes (m_h^*) and electrons (m_e^*), respectively, and are given by

$$\Delta E_{VBM} = -\frac{h^2}{8m_h^* R^2} \qquad \Delta E_{CBM} = \frac{h^2}{8m_e^* R^2} \tag{3.1}$$

, where h is Planck’s constant; and R is the radius of the quantum dot. The effective masses of the holes and electrons are obtained from a free electron-like parabolic fit to band extrema, along the crystalline momentum vector with the most band dispersion. Since m_h^* of bulk CdSe has been reported to be three times heavier than m_e^*,[26] the effective mass approximation predicts the downward shift of the VBM to be roughly three times smaller than the upward shift of the CBM. For example, Equation (3.1) predicts a ΔE_{VBM} of -0.19, -0.46, and -0.76 eV and a ΔE_{CBM} of 0.66, 1.6, and 2.6 eV for 4.2, 2.7, and 2.1 nm diameter quantum dots, respectively. The experimentally measured changes in ΔE_{VBM} with quantum dot radius are much smaller than those calculated using Equation (3.1). However, this simple model is known to be inaccurate and overestimate the quantum confinement effect. More advanced calculations based on first principles predict that $-\Delta E_{VBM} \approx \Delta E_{CBM}$ as the size of the CdSe quantum dot is decreased.[27] Clearly, a difference in quantum confinement between the electron and the hole cannot explain the results observed here.

To preferentially pin the HOMO of the CdSe quantum dots to the substrate VBM or Fermi level, there must be strong electronic interaction between CdSe and ZnO electronic levels. This is possible because the MPA linkers are not expected to form a tightly packed monolayer coating on the CdSe quantum dot surface. Indeed, high resolution transmission electron micrographs of CdSe quantum dots adsorbed on ZnO show an abrupt transition between the $(10\bar{1}0)$ lattice planes of ZnO and the (111) lattice planes of the CdSe quantum dot. This implies that the CdSe quantum dot and the ZnO surface are at least within an approximate distance of one ZnO $(10\bar{1}0)$ lattice spacing, 0.29 nm.[8] The precise mechanism of this energy pinning is not understood. This observation cannot be positively attributed to Fermi level pinning because the position of the Fermi level within the band gap of the isolated CdSe quantum dot is not known and is strongly affected by the surface chemistry. In addition, alignment of the vacuum level across the interface is not observed; instead, there is a small interfacial dipole (0.2-0.3 eV) that acts to make electron injection from CdSe into ZnO more favorable. An important result of the observed pinning is that changing the size of the CdSe quantum dots leads to the tuning of the LUMO levels in CdSe with respect to the CBM of ZnO. The interfacial energy alignment summarized in Fig. 3-3 suggests that higher lying levels above the first excitonic transition might be important for electron injection from the larger dot sizes examined here.

3.4 Conclusions

In summary, UPS measurements were carried out for sub-monolayer coverages of CdSe quantum dots adsorbed on single crystal ZnO $(10\bar{1}0)$ surfaces via 3-mercaptopropionic acid linkers. The valence band maximum of the CdSe quantum dots was found at about 1.2 eV above the valence band maximum of ZnO, nearly independent of the size of the quantum dots in the diameter range of 2.1-4.2 nm. The pinning of the CdSe valence band maximum to that of ZnO is attributed to strong electronic interaction between the two semiconductor materials. Thus, varying the quantum dot size mainly tunes the alignment of the conduction band minimum of CdSe with that of the ZnO surface. In addition, an interfacial dipole of about 0.2 eV was measured and found to make electron injection from CdSe quantum dots to ZnO more favorable. The energy alignment determined here has important implications for the rational design of quantum dot-sensitized solar cells.

3.5 References

1. Gregg, B. A., *J. Phys. Chem. B* **2003**, *107*, 4688-4698.
2. O'Regan, B.; Grätzel, M., *Nature* **1991**, *353*, 737-740.
3. Baxter, J. B.; Aydil, E. S., *Appl. Phys. Lett.* **2005**, *86*, 053114(3).
4. Law, M.; Greene, L. E.; Johnson, J. C.; Saykally, R.; Yang, P., *Nat. Mater.* **2005**, *4*, 455-459.
5. Vogel, R.; Pohl, K.; Weller, H., *Chem. Phys. Lett.* **1990**, *174*, 241-246.
6. Vogel, R.; Hoyer, P.; Weller, H., *J. Phys. Chem.* **1994**, *98*, 3183-3188.
7. Yu, P.-R.; Zhu, K.; Norman, A. G.; Ferrere, S.; Frank, A. J.; Nozik, A. J., *Langmuir* **1998**, *14*, 3153-3156.
8. Leschkies, K. S.; Divakar, R.; Basu, J.; Enache-Pommer, E.; Boercker, J. E.; Carter, C. B.; Kortshagen, U. R.; Norris, D. J.; Aydil, E. S., *Nano Lett.* **2007**, *7*, 1793-1798.
9. Robel, I.; Subramanian, V.; Kuno, M.; Kamat, P. V., *J. Am. Chem. Soc.* **2006**, *128*, 2385-2393.
10. Liu, D.; Kamat, P. V., *J. Phys. Chem.* ***1993***, *97*, 10769-10773.
11. Schaller, R. D.; Klimov, V. I., *Phys. Rev. Lett.* **2004**, *92*, 186601(4).
12. Ellingson, R. J.; Beard, M. C.; Johnson, J. C.; Yu, P.-R.; Micic, O. I.; Nozik, A. J.; Shabaev, A.; Efros, A. L., *Nano Lett.* **2005**, *5*, 865-871.
13. Olson, D. C.; Piris, J.; Collins, R. T.; Shaheen, S. E.; Ginley, D. S., *Thin Solid Films* **2006**, *496*, 26-29.
14. Diebold, U.; Koplitz, L. V.; Dulub, O., *Appl. Surf. Sci.* **2004**, *237*, 336-342.

15. Colvin, V. L.; Alivisatos, A. P.; Tobin, J. G., *Phys. Rev. Lett.* **1991**, *66*, 2786-2789.
16. Wu, P.-J.; Tsuei, K.-D.; Hsieh, M.-T.; Wei, K.-H.; Liang, K. S., *Phys. Rev. B* **2007**, *75*, 115402(8).
17. Lee, J. R. I.; Meulenberg, R. W.; Hanif, K. M.; Mattoussi, H.; Klepeis, J. E.; Terminello, L. J.; van Buuren, T., *Phys. Rev. Lett.* **2007**, *98*, 146803(4).
18. Reiss, P.; Bleuse, J.; Pron, A., *Nano Lett.* **2002**, *2*, 781-784.
19. Yu, W. W.; Qu, L.-H.; Guo, W.-Z.; Peng, X.-G., *Chem. Mater.* **2003**, *15*, 2854-2860.
20. Aldana, J.; Wang, Y. A.; Peng, X.-G., *J. Am. Chem. Soc.* **2001**, *123*, 8844-8850.
21. Lüth, H.; Rubloff, G. W.; Grobman, W. D., *Solid State Comm.* **1976**, *18*, 1427-1430.
22. Moulder, J. F.; Stickle, W. F.; Sobol, P. E.; Bomben, K. D.; *Handbook of X-ray Photoelectron Spectroscopy*; Physical Electronics, Inc.: Eden Prairie, 1995.
23. Ozawa, K.; Sawada, K.; Shirotori, Y.; Edamoto, K., *J. Phys.: Condens. Matter* **2005**, *17*, 1271-1278.
24. Franceschetti, A.; Zunger, A., *Phys. Rev. Lett.* **2007**, *98*, 915-918.
25. Brus, L., *J. Phys. Chem.* **1986**, *90*, 2555-2560.
26. Dalven, R., *Phys. Stat. Sol. B* **1971**, *48*, K23-K26.
27. Wang, L.-W.; Li, J., *Phys. Rev. B* **2004**, *69*, 153302(4).

Chapter 4. Ligand Dependent Alignment at Interfaces of Lead Selenide Quantum Dots and Oxide Surfaces

4.1 Introduction

Quantum dot solar cells are an important branch of solar energy research. Semiconductor nanoparticles have desirable properties as light absorbers, such as strong oscillator strength near the band edge and size-tunable band gaps. Colloidal quantum dots, in particular, are attractive for their easy incorporation with solution processing and high control through synthetic methods of nanoparticle crystallinity and monodispersity. Lead selenide is a promising nanomaterial with several well developed syntheses for high quality dots,[1, 2] the availability of which has prompted extensive theoretical research, an IR band gap to extend the photovoltaic effect into portions of the solar spectrum not accessible by most organic chromophores, and demonstrated multiple exciton generation,[3,4] which has enhanced interest in PbSe for optoelectronic applications.

Several architectures exist for fabrication of quantum dot photovoltaic devices. Recent studies of bulk heterojunction cells containing PbSe quantum dots [5, 6] report very poor efficiencies, which can be partly attributed to the presence of long chain insulating ligands on the PbSe quantum dot surface. These ligand molecules, commonly oleic acid, trioctylphosphine oxide, or other long chain alkenes or amines, are necessary during the quantum dot synthesis to mediate particle growth and impart colloid stability. Although these surfactants can facilitate quantum dot deposition via solution casting, they present both spatial and electrical barriers to charge transfer. As such, solution phase ligand exchange reactions are sometimes used to introduce shorter ligands; however, these post-synthetic treatments reduce colloid stability and can leave the quantum dot surface vulnerable to degradation and oxidation.[7]

Another device geometry that has been explored for PbSe quantum dot solar cells is the Schottky diode, whereby a thin film of quantum dots is sandwiched between two electrodes.[8, 9] Once it was reported that exposing a PbSe quantum dot array to 1 M hydrazine led to removal of oleate ligands and dramatic increases in quantum dot film conductivity,[10] several groups began to pursue the use of post-deposition ligand treatments to improve the electrical characteristics of quantum dot films. The most common ligand treatments involve hydrazine and 1,2-ethanedithiol (EDT), though numerous studies exist for other simple amines and thiols.[9, 11, 12] It is observed that ligand treatments displace the weakly acid-bound oleate molecules from the quantum dot surface, leading to reduced inter-particle spacing and increased electronic coupling within the film.

Quantum dots can also be incorporated into solar cells as photosensitizers for wide band gap semiconductors such as ZnO and TiO_2, extending spectral response to visible and infrared wavelengths. This approach has been widely demonstrated for quantum dot materials like CdSe,[13, 14] CdS,[15, 16] CdTe,[17] InP,[18] InAs,[19] and PbS;[20, 21] however, only one study has reported using PbSe as a sensitizer for amorphous TiO_x.[22]

Efficient charge transfer at the interface between the two semiconductors, essential for photosensitization, is dependent upon favorable alignment of energy levels, the so-called “type II” band alignment. The excited state in the quantum dot donor must lie above the conduction band edge of the acceptor. Quantum dot size-dependent energy level structure is expected to have a large effect on the observed energy level offset between a semiconductor quantum dot and an oxide substrate. Studies have reported quantum dot size-dependent electron injection from CdSe [23] and PbS quantum dots [20, 24] to TiO_2 nanoparticles. Hyun *et al*. performed simple calculations of the band edge energies in for PbS and PbSe and plotted them against band edge values for TiO_2 from electrochemical measurements, predicting a size threshold for electron injection into TiO_2 of 4.3 nm and less than 1 nm for PbS and PbSe, respectively. The only report of the PbSe quantum dot -TiO_x interface [22] measured the onset of photocatalysis and predicted a PbSe quantum dot size threshold of about 8 nm for electron injection into TiO_x, estimating energy levels of one dot size from electrical measurements and extrapolating the size-dependent band offset by assuming equal confinement of electrons and holes, though recent calculations of the electronic structure of PbSe quantum dots suggest that hole states are much denser and less affected by quantum confinement than would be expected from the roughly equal carrier effective masses in bulk PbSe.[25] Clearly, reliable energy alignment measurements for these systems would be useful in optimizing device performance.

Photoemission measurements offer an excellent method to examine interfacial energy alignment.[26] The technique of ultraviolet photoelectron spectroscopy (UPS) is capable of measuring the density of states at a surface and has long been used to determine valence band offsets between substrates and thin films, monitoring sequential changes in the valence electronic structure during heterointerface formation as the overlayer is gradually deposited on the substrate.[27] However, its application has generally been limited to samples prepared *in vacuo*. In the last several years researchers have begun to use UPS to investigate interfacial alignment between organic chromophores and metal oxide electrode materials for dye-sensitized solar cells, the prototypical precursor to the quantum dot-sensitized solar cell.[28-30] Recent experiments in our lab showed the interfacial alignment of CdSe quantum dot-ZnO interfaces as a function of quantum dot size to exhibit a fixed valence band offset.[31] The demonstration of the technique for interfaces that are prepared outside of the vacuum chamber using wet chemical approaches should lead to much more research on energy alignment for quantum dot optoelectronics.

To investigate the issue of band alignment for quantum dot photosensitization model interfaces have been constructed of PbSe quantum dots on single crystal wide band gap oxide substrates, specifically ZnO $(10\bar{1}0)$ and rutile TiO_2 (110). The interfaces are prepared by dip coating, in analogy to methods used in actual device fabrication. The effect of ligand treatments with hydrazine and EDT on the interfacial energy alignment is investigated. Ligand molecules are expected to contribute to observed alignment by way of facilitating charge transfer through covalent linkages or introducing interfacial dipoles, as has been very recently reported for CdS-TiO_2 interfaces modified by benzenethiol derivatives.[32] The hydrazine and EDT ligand treatments are known to have dramatic effects on the electrical properties of quantum dot arrays, but no studies have previously examined their affect on the energy alignment between quantum dot films and an oxide substrate. In analogy to molecules the valence band maximum (VBM) and conduction band minimum (CBM) of the quantum dots are also refer to as highest occupied molecular orbital (HOMO) and lowest unoccupied molecular orbital (LUMO) levels.

The two substrates show very different behavior in directing the energy alignment with PbSe quantum dots. A very small shift of the HOMO vs. quantum dot size on ZnO after both hydrazine and EDT treatments is indicative of significant electronic interaction between the PbSe quantum dots and ZnO; in particular, EDT-treated PbSe films on ZnO display strong quantum dot valence band intensity enhancement due to nanoparticle-substrate coupling through the EDT molecules. In contrast, ligand-treated PbSe quantum dot films on TiO_2 show a quantum dot size-dependent valence band offset that is expected for weakly interacting interfaces, as well as a much smaller dependence of alignment on the specific ligand treatment used. In most of the cases presented the interfacial energy alignment, constructed using a combination of UPS and optical absorption measurements, suggests that injected electrons from PbSe quantum dots into either ZnO ($10\bar{1}0$) or TiO_2 (110) could only originate from states above the quantum dot LUMO.

4.2 Experimental

Oleate-capped PbSe quantum dots were prepared from a PbO precursor according to published procedures.[1, 33] Mean particle sizes were determined from optical absorption measurements in carbon tetrachloride solutions. The lowest energy excitonic absorption peak positions were λ = 1108 and 2015 nm, corresponding to particle diameters of D = 3.4 and 6.7 nm, respectively, as determined from the published calibration curve of Dai *et alia*.[34] The size distribution of the quantum dot batches was determined to be ± 5% from the full-width-at-half-maximum of the first exciton peak.

All film depositions and ligand treatments were performed in an argon glove box. One-side polished ZnO wafers of $(10\bar{1}0)$ orientation and two-side polished rutile TiO_2 crystals of (110) orientation were purchased from MTI Corporation. Clean ZnO crystals were etched 5 minutes in 1 mM HNO_3, and clean TiO_2 crystals were etched 30-60 minutes in 1 M HCl while under UV ($h\nu$ = 254 nm) illumination, following the preparation by Lu *et al*.,[35] immediately before transfer to the glove box. Nanoparticle films were prepared by dip coating in colloidal dispersions in hexanes and withdrawn from the dispersion at a rate of 1 cm/s. Dispersion concentrations were 1 mg/mL unless otherwise noted. This concentration was chosen to give sub-monolayer coverage on the substrate. Quantum dot coverage in these experiments was not quantified except by comparison to atomic force microscope images taken in our lab for identically prepared samples.[36] Hydrazine (N_2H_4) treated samples were submerged in a 1 M hydrazine solution in acetonitrile for 30-60 minutes, while 1,2-ethanedithiol (EDT) treated samples were submerged in 0.1 M EDT solutions in acetonitrile for 1-40 minutes. The ligand treatment durations were selected such that oleate removal from the sub-monolayer film was complete as determined by FTIR measurements. All ligand-treated quantum dot films were rinsed with acetonitrile to remove weakly adsorbed species and mounted on sample holders before being removed from the glove box. During the transfer to the ultrahigh vacuum chamber, samples were exposed to air for < 10 s; however, no noticeable oxidation of either Pb or Se was observed in x-ray photoelectron spectroscopy (XPS) measurements performed on identically prepared samples.

All UP spectra were collected at room temperature in an ultrahigh vacuum spectrometer equipped with a hemispherical electron energy analyzer (Phi 5400). He-I radiation ($h\nu = 21.2$ eV) was used as the UV light source, and the lamp power was set at 25 W. Incident light was 50° from the sample normal, and photoelectrons were collected along the sample normal direction with an analyzer pass energy of 4.45 eV and a sample bias of -8.0 V.

4.3 Interfacial Alignment from Photoemission Measurements

Substrate features are not observed in the spectra after quantum dot deposition. This is due in part to attenuation by the quantum dot overlayer, whereby even a single layer of dots exceeds the electron escape depth at all kinetic energies accessed in these experiments. This consideration prompted the desire for measurements of sub-monolayer quantum dot films. However, the substrate features are further attenuated by excess oleic acid molecules that are introduced onto the substrate during the dip coating process. It is well known that long fatty acids form self-assembled monolayers on oxide surfaces,[37] and therefore this adsorption is inevitable. Excess oleic acid molecules will always be present in the quantum dot dispersions due to equilibrium between bound and free molecules in solution, so even extra post-synthesis cleaning of the dots through many precipitation and centrifugation cycles will not eliminate this monolayer formation on the substrate. Further, it was observed through control experiments (i.e. without quantum dots) that the ligand treatments do not remove a significant portion of oleic acid monolayers from the ZnO substrate.

Alignment is determined by referencing to the Fermi level of the substrate, which is 3.2 eV above the VBM for ZnO ($10\bar{1}0$), and 2.7 eV above the VBM for TiO_2 (110). It is presumed that Fermi level equilibration at the interface takes place by way of the large density of surface defect states on the substrates. The lack of visible substrate features in spectra of sub-monolayer quantum dot films contrasts previous experiments that determined the alignment for 3-mercaptopropionic acid-capped CdSe quantum dots on ZnO ($10\bar{1}0$) as a function of dot size. In those experiments the ligand treatment of the dots was carried out in a separate solution phase exchange prior to quantum dot deposition on the substrate. The attenuation of substrate features at low quantum dots coverages did not occur, allowing for observation of both substrate and overlayer valence band edges in a single spectrum. This distinction highlights a key difference between the two methods of quantum dot ligand treatment: the post-deposition treatment of films allows for easier processing of the materials, but at a cost of altering the electronic structure of the interface. The presence of insulating fatty acid molecules on the oxide substrate will hinder charge transfer between the semiconductors. This effect may be enhanced in thicker (multilayer) quantum dot films because of geometric frustration; that is, oleic acid molecules can squeeze between close-packed quantum dots.

Changes were followed in the work function of the sample, determined by the position of the vertical secondary electron threshold at the low kinetic energy end of the spectrum. Monitoring this value allowed for observation or exclusion of sample charging, the presence of which would invalidate the assumption of Fermi level alignment in samples containing quantum dots. Samples of untreated (oleic acid-capped) quantum dots always displayed severe charging, whereas ligand-treated samples did not ever have charging problems. Also, the spectrum of the oleic acid monolayer on ZnO did not exhibit charging. These observations point to the huge amount of oleic acid present in the untreated samples, which was also confirmed by XPS (not shown).

The work function of the sample can also elucidate the presence of interfacial dipoles, which have an important effect on charge transfer between two semiconductors. In general the vacuum level offset between two samples is a result of multiple contributions, including charge redistribution from chemical bonding, band bending in the substrate and surface or interfacial dipoles.[26] The role of substrate band bending on the vacuum level offset can be removed by subtracting core level shifts measured using XPS. Though no XPS measurements were taken for the samples discussed here, it is assumed that band bending contributes $\leq$ 0.1 eV to the vacuum level shift. In a previous study of alignment at CdSe quantum dot and ZnO $(10\bar{1}0)$ interfaces containing 3-mercaptopropionic acid (MPA) linker molecules, larger absolute vacuum level shifts were observed (0.3 eV), and band banding only accounted for 0.1 eV of the shift.[31] The MPA molecule is expected to have a stronger surface dipole effect than either hydrazine or EDT due to oriented attachment; that is, the carboxylate group has a stronger binding affinity for the oxide surface than thiolates. In all samples discussed in this work the vacuum level shifts are $\leq$ 0.2 eV. The consequences of vacuum level offsets on the measured energy alignment will be discussed in the sections below.

The work function of the bare substrates was measured to be 3.8 eV for both ZnO $(10\bar{1}0)$ and TiO_2 (110). This is significantly lower than the values reported for surfaces prepared *in vacuo*, around 4.5 eV [38] and 4.2 eV [39] for ZnO $(10\bar{1}0)$ and TiO_2 (110), respectively, the difference being that the surfaces in these experiments were prepared at ambient pressure, in accordance with wet chemistry techniques utilized in the preparation of colloidal quantum dot solids. As such, adsorption of adventitious hydrocarbons is responsible for the reduced work functions of the substrates. However, it is expected that the degree of contamination due to hydrocarbon dust is equivalent for all samples discussed here and does not affect the results of the comparisons presented.

4.4 Hydrazine Treatments on Zinc Oxide Surfaces

The valence band of the ZnO substrate is strongly affected by hydrazine exposure. Figure 4-1 a) shows UP spectra of a clean ZnO $(10\bar{1}0)$ crystal and one that has been exposed to 1 M hydrazine in acetonitrile for 170 minutes. The dotted trace shows the structure of the ZnO valence band edge, with the VBM located at 3.2 eV below the Fermi level. The sharp kink in the density of states delineates between the filled band and the exponential tail of surface defect states. The valence band of ZnO consists mostly of contributions from O 2p states in the 3-6 eV region, with additional contributions from Zn 4s in the 6-9 eV region.[40] The hydrazine treatment of ZnO is seen to have two major effects on this portion of the spectrum. First is reduction of the valence band intensity in the 3-6 eV region, which suggests a loss of oxygen from the surface. The second effect is the loss of VBM structure, instead giving way to a steady exponential tail of defect states at binding energies below 5 eV. Hydrazine is not found to be incorporated on the treated surface, and thus the changes in the spectrum reflect modification of the ZnO electronic structure. Hydrazine treatment of ZnO both reduces the surface and erodes the structure of the valence band, and this affects the electronic coupling between the ZnO substrate and PbSe quantum dots, as will be discussed below.

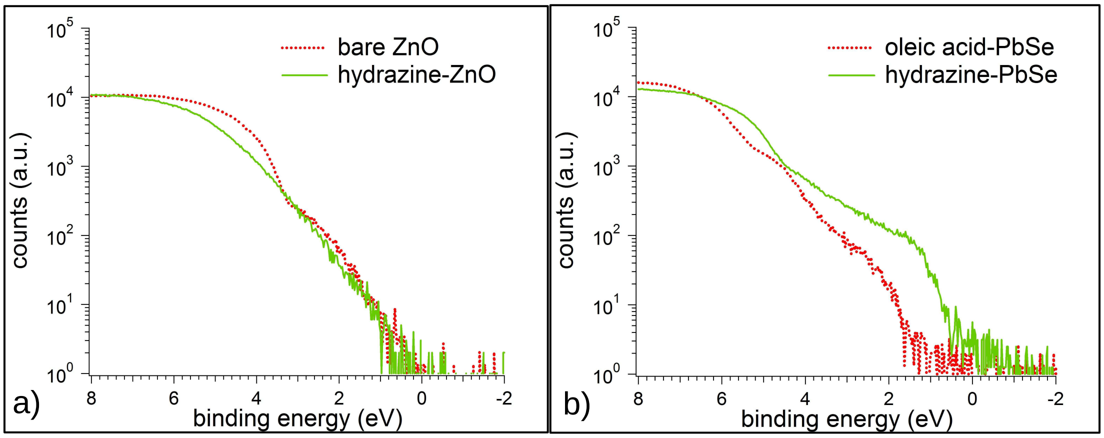

Figure 4-1. Valence region of UP spectra showing the effects of the hydrazine treatment on ZnO and oleic acid-capped PbSe quantum dots. Panel a) shows a spectrum of bare ZnO $(10\bar{1}0)$ crystal and one that has been exposed to 1 M hydrazine in acetonitrile for 170 minutes. Panel b) shows D = 3.4 nm oleic acid-capped PbSe quantum dots on a ZnO $(10\bar{1}0)$ surface before and after a 57 minute treatment in 1 M hydrazine in acetonitrile. Quantum dot films were prepared by dip coating from a 1 mg/mL dispersion. E = 0 on the binding energy scale corresponds to E_f.

Hydrazine treatment also dramatically changes the photoemission spectrum of the PbSe quantum dots, as shown in Fig. 4-1 b). Before treatment (dotted trace) the valence band edge of the quantum dots is not visible. It is completely attenuated by the thick shell of oleic acid ligands on the PbSe surface. This untreated sample also exhibited charging effects, which is consistent with the insulating nature of the ligands. After removal of the oleic acid capping molecules by treatment in hydrazine emission is seen from the quantum dot valence band. Intensity in the region above the VBM of the ZnO substrate is increased, tailing off at binding energies below 1 eV. This is reasonable since the band gap of the D = 3.4 nm PbSe quantum dots in Fig. 4-1 b) is 1.1 eV, and the Fermi level must lie within the energy gap.

Figure 4-2 a) shows UP spectra of the valence band region as a function of surface coverage of 3.4 nm PbSe quantum dots on the ZnO surface. The systematic variation in intensity with increasing concentration of the quantum dot dispersion used for dip coating allows assignment of the features at low binding energies to the valence band of the PbSe quantum dots. At higher coverages of nanoparticles a tail of finite counts across the Fermi level is observed; this is due to a thermal distribution. The substrate (small dotted) trace is that of a bare ZnO crystal subjected to the same hydrazine treatment (1 M in acetonitrile) as the samples containing quantum dots. In view of the ligand interaction with the substrate it was determined that the ligand-treated substrate, as opposed to the untreated substrate, is a more accurate representation of the electronic platform with which the dots interact. Control

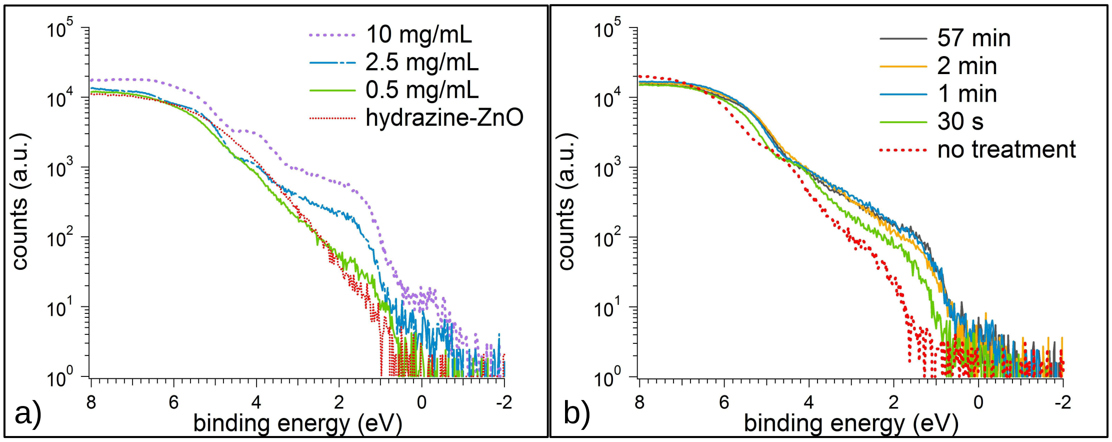

Figure 4-2. UP spectra of hydrazine-treated D = 3.4 nm PbSe quantum dots on a ZnO $(10\bar{1}0)$ surface. Panel a) shows variation of quantum dot coverage by the dispersion concentration used for dip coating. For comparison a hydrazine-treated ZnO substrate is shown. Panel b) shows the effect of removal of oleic acid from the surface of PbSe quantum dots with increasing treatment time in 1 M hydrazine.

experiments show that hydrazine treatment doesn't remove a significant portion of an oleic acid monolayer on ZnO, indicating that the oleic acid monolayer presents a barrier between the hydrazine and ZnO substrate. However, the hydrazine treatment does remove oleic acid from the PbSe quantum dot surface, and it is expected that the surface area of ZnO immediately surrounding the oleic acid-stripped quantum dot is able to interact with the hydrazine molecules in solution.

The HOMO level of the PbSe quantum dots was determined for all samples by the lowest energy peak in the second derivative of the measured spectrum, or the inflection point of the low energy intensity shelf, showing up between about 0.4-1.2 eV in Fig. 4-2 a). The HOMO for hydrazine-treated 3.4 nm PbSe quantum dots shown in Fig. 4-2 a) was found to exhibit a coverage-dependent shift, starting off at 0.7 eV for lower coverages (obtained from dispersion concentrations ≤ 1 mg/mL) and jumping to 0.9 eV for higher coverages (dispersion concentrations ≥ 2.5 mg/mL). Atomic force microscope images show that dip coating from a 1 mg/mL quantum dot dispersion onto a single crystal substrate result in films that correspond to 20-30% of a monolayer, with mostly isolated islands of single layers of dots.[36] Pronounced quantum dot features that emerge in the UP spectra for dispersion concentrations of 2.5 mg/mL (and higher) suggest that this coverage corresponds nearly to a complete monolayer. Correlating the structural information from atomic force microscope imaging and the energetic information from UPS, the 0.7 eV quantum dot HOMO obtained at low coverages can be viewed as the “interfacial” value of the quantum dot energy level position, while the 0.9 eV quantum dot HOMO can be viewed as the “bulk-like” value. This phenomenon of a coverage-dependent position for the VBM or HOMO is well known from UPS studies of heterointerface formation.[41] Since the interest lies in the interfacial energy alignment between PbSe quantum dots and the oxide substrate, all comparisons will be made using samples fabricated by dip coating from a 1 mg/mL quantum dot dispersion, concentrating on the interfacial alignment, where each quantum dot is in direct contact with the substrate.

It has been observed that removal of oleic acid ligands by hydrazine-acetonitrile solutions occurs on the time scale of several minutes, with complete removal of oleate from two-dimensional films by 15 minutes. Congruent with the oleate removal a systematic red shift of the lowest energy excitonic transition versus hydrazine treatment time occurred, the shift being complete after 25 minutes of treatment.[36] Figure 4-2 b) shows UP spectra of the valence band region of 3.4 nm PbSe quantum dots on ZnO as a function of treatment time in 1 M hydrazine in acetonitrile. As discussed above, before hydrazine treatment the HOMO of PbSe quantum dots is not visible. Though the shape of the dotted trace appears to somewhat match the intensity profile of the other traces, there is no sharp inflection point on the low binding energy intensity shelf, in contrast to observations on all samples of ligand-treated quantum dot films. Additionally, estimating the approximate inflection point by eye leads one to a HOMO of about 1.7 eV, which makes no physical sense for nanoparticles with an optical band gap of 1.1 eV. After 30 seconds of treatment the HOMO is at 1.0 eV; at 1 and 2 minutes the HOMO shows up at 0.8 eV; and after complete reaction with hydrazine (1 hour) the HOMO has reached the interfacial value of 0.7 eV. This shift of the quantum dot HOMO does not indicate a red-shift of the excitonic energy gap; the total magnitude of the red shift observed by Williams *et al.* is just over 0.1 eV, which is the limit of the energy resolution of this experiment. Rather, the shift indicates oleate removal and the reversal of attenuation of the quantum dot valence band.

The dependence on particle size of the position of the PbSe quantum dot HOMO at the ZnO $(10\bar{1}0)$ interface gives insight about the mechanism of energy alignment. Figure 4-3 shows UP spectra of hydrazine-treated quantum dot films on ZnO for two different dot sizes, having diameters of 3.4 nm and 6.7 nm and corresponding optical band gaps of 1.1 eV and 0.6 eV, respectively. The position of the interfacial HOMO is measured to be at 0.7 eV for 3.4 nm dots and 0.6 eV for 6.7 nm dots. Noting the difference in band gap of the two different batches of dots, about 0.5 eV, this implies that changing the quantum dot size results in a much larger shift of the quantum dot LUMO with respect to the ZnO substrate. Given the roughly equal effective masses for electrons and holes in bulk PbSe,[42] this unequal distribution of the energy shift between HOMO and LUMO is somewhat unexpected. Yet, recent structural calculations have predicted that hole effective masses are heavier than expected in PbSe quantum dots.[25, 43] However, the relatively fixed HOMO alignment observed here suggests strong electronic interaction with the ZnO substrate.

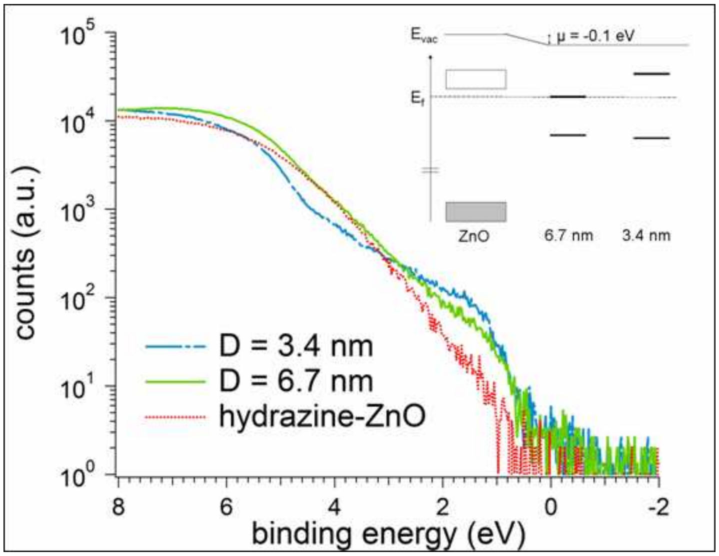

Figure 4-3. Energy alignment of hydrazine-treated PbSe-ZnO interfaces vs. quantum dot size. The inset summarizes the interfacial band offsets determined from UPS. The measured HOMO positions for D = 3.4 nm and 6.7 nm are 0.7 eV and 0.6 eV, respectively, with respect to the Fermi level. The double bar on the energy axis represents a scale discontinuity. The vacuum level offset is depicted as an interfacial dipole μ = -0.1 eV.

The relatively fixed position of the quantum dot HOMO vs. dot size for hydrazine-treated films of PbSe quantum dots on ZnO is a direct result of hydrazine's chemical interaction with the ZnO substrate. This fixed valence band offset is in contrast to measurements of hydrazine-treated films of PbSe quantum dots on TiO_2, which do show size dependence of the quantum dot HOMO in accord with the changing quantum dot band gap; these results will be reviewed in detail below. The strong electronic interaction between hydrazine treated PbSe quantum dots and ZnO may result from enhanced reactivity of the reduced ZnO surface, but more work is needed to clarify this point. A vacuum level offset of -0.1 eV is observed at the hydrazine-treated PbSe-ZnO interface; the work function of the bare ZnO substrate is 3.8 eV, while the average work function of hydrazine-treated PbSe quantum dot films on ZnO $(10\bar{1}0)$ is 3.7 ± 0.1 eV. Hydrazine has not been found to be incorporated in the samples containing quantum dots, which may be a result of the ultrahigh vacuum experimental conditions. Previous experiments have noted the weak binding ("physisorption") of hydrazine molecules to quantum dot films.[10, 12] Thus, it is expected that the hydrazine-treated sample surface consists of patches of ligand-stripped quantum dots and areas of ZnO covered with oleic acid molecules. An oleic acid monolayer on ZnO did not change the work function from the measured value on the bare substrate (3.8 eV). The small work function change observed on the hydrazine treated PbSe quantum dot films on ZnO might reflect the work function of PbSe, but this value has never been reported in the literature for single crystal or polycrystalline PbSe.

The interfacial energetic alignment measured for hydrazine-treated PbSe quantum dots on ZnO ($10\bar{1}0$) is summarized in the inset of Fig. 4-3. The positions of the quantum dot HOMO from UPS measurements are 0.6 eV for 6.7 nm PbSe and 0.7 eV for 3.4 nm PbSe. The VBM of ZnO, from UPS measurements of the clean substrate, is at 3.2 eV. The alignment of the excited states is implied from optical absorption measurements. The band gap of ZnO is 3.4 eV, and the excitonic transition energies for the two sizes of dots are 0.6 eV and 1.1 eV for 6.7 nm and 3.4 nm PbSe quantum dots, respectively. The measured vacuum level offset of -0.1 eV can as a first approximation be treated as an interface dipole and is shown in the energy level diagram.

Since features from the substrate are not observed in UP spectra of samples containing quantum dots, the alignment of the measured quantum dot levels to the Fermi level of the bulk substrate is assumed, and a few statements must be made about this assumption. It was shown above that hydrazine treatments reduced surface oxygen from the substrate, and that this reduction eroded the VBM structure. However, the work function of the ZnO crystal did not change after hydrazine treatment, and therefore it is expected that the bulk Fermi level is not affected by the hydrazine exposure. That is, hydrazine only changes the doping level of the ZnO crystal within the top few atomic layers. To place the VBM of ZnO at 3.2 eV in the inset of Fig. 4-3 is a more dubious assumption, given the effect of hydrazine on the valence band structure of the substrate surface. Though, it is obvious from Fig 4-1 a) that the positions of the valence levels of ZnO are not significantly shifted along the energy axis.

The energetic alignment displayed in the energy diagram in the inset of Fig. 4-3 suggests that the LUMO's of the quantum dots are very near the CBM of ZnO, with the LUMO of 6.7 nm dots right at the Fermi level and below the ZnO CBM. However, the reported quantum dot energy gaps are excitonic transition energies, and it is important to distinguish between the optical vs. transport band gap. The optical gap is smaller than the transport gap by the amount of the exciton binding energy, which is generally dependent on particle size but expected to be on the order of tens of meV for PbSe nanoparticles due to the large dielectric constant of bulk PbSe.[44] Even so, the interfacial energy alignment reported here should give insight on the operation of photovoltaic devices fabricated using such quantum dot films. It is obvious from the energy diagram that electron injection from the photoexcited quantum dot LUMO to the ZnO conduction band cannot occur for hydrazine-treated 6.7 nm PbSe particles; instead, higher lying excited states would have to be involved for interfacial charge transfer, which should, for instance, be reflected in the wavelength-dependent spectral response of a photovoltaic device.

4.5 One, Two-Ethanedithiol Treatments on Zinc Oxide Surfaces

Ligands treatments of PbSe quantum dots on ZnO $(10\bar{1}0)$ using EDT provide several important distinctions from the hydrazine-ZnO system. First, the EDT ligand molecules bind to the ZnO surface, as opposed to the more chemical etch-like interaction occurring with hydrazine. UP spectra of the ZnO

($10\bar{1}0$) substrate before and after exposure to 0.1 M EDT in acetonitrile for 1 minute are shown in Figure 4-4 a). The thiol peak around 3 eV is a prominent feature in the spectrum of the treated substrate, as is some attenuation of the ZnO valence band intensity.[45] The increase of the substrate work function by 0.1 eV after EDT adsorption is consistent with reported interactions between ZnO and sulfur compounds.[46] Though, the molecular structure of the EDT-ZnO interface is not known, and there is likely a combination of mono- and bidentate coordination of the sulfur atoms at the surface.

Figure 4-4 b) shows UP spectra of the valence band region of EDT treated 3.4 nm PbSe quantum dot films as a function of dispersion concentration used for dip coating on the ZnO ($10\bar{1}0$) surface. From the growth in valence band intensity it is obvious that the quantum dot dispersion concentration directly correlates to the amount of PbSe on the surface. The quantum dot HOMO displays coverage dependence, taking on an interfacial value of 0.5 eV for lower coverages (obtained from dispersion concentrations ≤ 1 mg/mL) and shifting to 0.7 eV for higher coverages (dispersion concentrations ≥ 2.5 mg/mL). Two important characteristics of the EDT-PbSe-ZnO system distinguish it from the HYD-PbSe-ZnO system discussed above. First, the thiol peak at 3 eV is present, indicating binding of the EDT molecule to the nanoparticle surface. The presence of EDT on the sample surface leads to an increase in work function; the EDT-treated ZnO ($10\bar{1}0$) substrate (without PbSe) has a work function of 3.9 eV, while the average work function of the EDT-treated PbSe quantum dot films on ZnO is 4.0 ± 0.1 eV. The augmentation

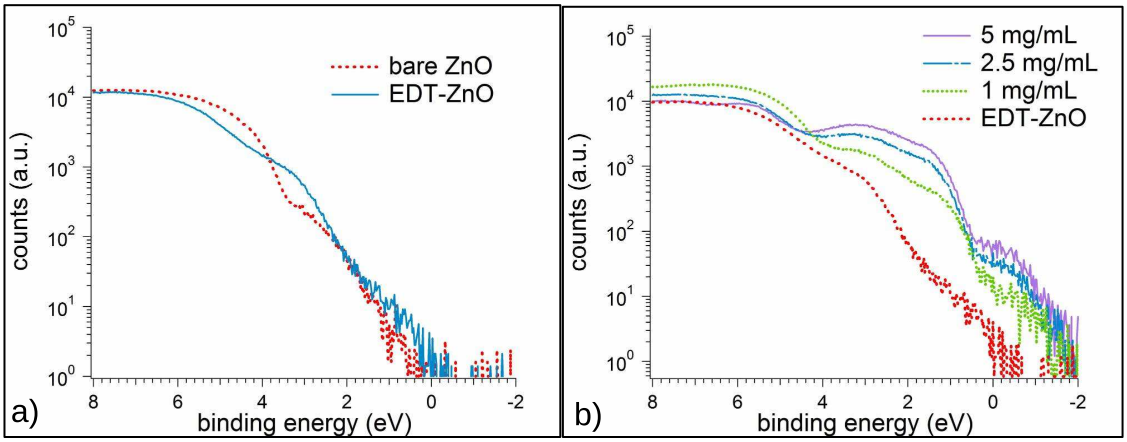

Figure 4-4. Valence region of UP spectra showing the effects of the EDT treatment on ZnO and oleic acid-capped PbSe quantum dots. Panel a) shows a spectrum of bare ZnO $(10\bar{1}0)$ crystal and one that has been exposed to 0.1 M EDT in acetonitrile for 1 minute. Panel b) shows spectra of EDT-treated films of 3.4 nm PbSe quantum dots on ZnO vs. concentration of quantum dot dispersion used for dip coating. The spectrum of the EDT-treated substrate (dotted trace) is shown for comparison. E = 0 corresponds to E_f.

of the work function shift between samples with and without quantum dots reflects an increased concentration of EDT on samples containing quantum dots, since the EDT molecules have many more potential binding sites than on the relatively flat single crystal surface. Second, the relative valence band spectral intensity of PbSe quantum dots is much higher, by about a factor of three, than for a hydrazine-treated film of equivalent quantum dot coverage. This variation of intensity is not due to an increase in quantum dot coverage on the surface, as the dip coating method was found to give reproducible intensities within ± 25% for identically prepared quantum dot films. Furthermore, this dramatic enhancement of valence band intensity is not observed in EDT-treated PbSe quantum dot films on TiO_2, where the ligand interaction with the substrate is much weaker, as will be discussed in detail below. The enhancement of valence band intensity indicates strong electronic coupling with the ZnO substrate that is mediated by the EDT molecules.

Interfacial alignment as a function of quantum dot size was measured for sub-monolayer films of EDT-treated 3.4 nm and 6.7 nm diameter PbSe quantum dots on ZnO $(10\bar{1}0)$ and is shown in Figure 4-5. This system exhibits no shift of the HOMO with changing nanoparticle size, with both sizes displaying a HOMO binding energy of 0.5 eV. Size-independence of the HOMO suggests strong electronic coupling between the PbSe quantum dots and the ZnO substrate that is mediated by EDT molecules on the surface. Since it was shown above that EDT binds strongly to ZnO, and the strong interaction of thiols with II-VI and IV-VI quantum dot surfaces is well known,[11, 47] it is

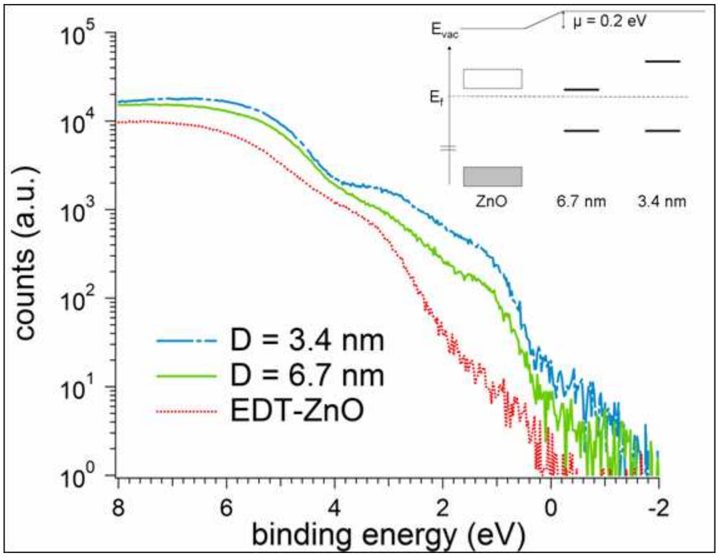

Figure 4-5. Energy alignment of EDT-treated PbSe-ZnO interfaces vs. quantum dot size. The inset summarizes the interfacial band offsets determined from UPS. The measured HOMO position for D = 3.4 nm and 6.7 nm is 0.5 eV with respect to the Fermi level. The double bar on the energy axis represents a scale discontinuity. The vacuum level offset is depicted as an interfacial dipole μ = 0.2 eV.

probable that some of the adsorbed EDT is bound to both PbSe and ZnO, acting as a molecular linker across which wavefunction density is delocalized and through which charge can be transferred. This strong electronic coupling can also explain the enhancement of valence band intensity observed in this system. From intensity differences it appears in Fig. 4-5 that the coupling between the 3.4 nm dots and ZnO is slightly stronger than for the 6.7 nm dots, which may be related to differences in the density of state profiles of the two quantum dot sizes.

The interfacial alignment measured for the EDT-PbSe-ZnO system is depicted in the energy diagram in the inset of Figure 4-5. The HOMO for both sizes of EDT-treated PbSe quantum dots is 0.5 eV below the Fermi level. Using optical gaps from absorption measurements to infer the alignment of the quantum dot LUMO's and the ZnO CBM leads to an offset of -0.1 eV for 6.7 nm dots and 0.4 eV for 3.4 nm dots. The measured vacuum level offset of 0.2 eV is placed at the PbSe quantum dot-ZnO interface and meant to suggest an interfacial dipole. It is interesting to note that, even with the improved alignment situation for the EDT- vs. hydrazine-treated PbSe quantum dot films, electron injection from the lowest excitonic state in 6.7 nm PbSe quantum dots to the ZnO conduction band will only occur with low efficiency if at all. In theory these energy alignment measurements predict a quantum dot band gap threshold of 0.7 eV for interfacial charge transfer.

4.6 Comparisons to Treatments on Titanium Dioxide Surfaces

UPS data of interfacial energy alignment for ligand-treated quantum dot films on TiO_2 (110) indicate that PbSe quantum dots do not interact strongly with the TiO_2 substrate, as opposed to the ZnO ($10\bar{1}0$) substrate, resulting from weak electronic interactions that the hydrazine and EDT ligands have with the TiO_2 valence band. Figure 4-6 a) shows UP spectra of hydrazine-treated sub-monolayer PbSe quantum dot films on TiO_2 as a function of particle size. Here, in clear contrast to the ZnO system, there is strong size-dependence of the quantum dot HOMO that is in accord with the different optical energy gaps of 0.6 eV for the larger dots and 1.1 eV for the smaller dots. The HOMO of 6.7 nm and 3.4 nm dots is located at 0.6 eV and 0.9 eV below the Fermi level, respectively. Size-dependence of the quantum dot HOMO was also noted for EDT-treated PbSe quantum dot films on TiO_2 (not shown), with values of 0.6 eV and 0.8 eV for 6.7 nm dots and 3.4 nm dots, respectively. The size dependence of the nanoparticle HOMO measured here suggests an energy alignment scheme that is more closely in line with vacuum level alignment, generally observed for weakly interacting heterointerfaces.[26]

In addition to dot size dependence of the PbSe quantum dot HOMO several key differences between ligand-treated PbSe quantum dot films on ZnO ($10\bar{1}0$) vs. TiO_2 (110) are illuminated by the UPS data that strongly suggest that the nanoparticle-substrate interaction is much weaker in the TiO_2 systems. First, there is a smaller shift of the PbSe quantum dot HOMO between the two

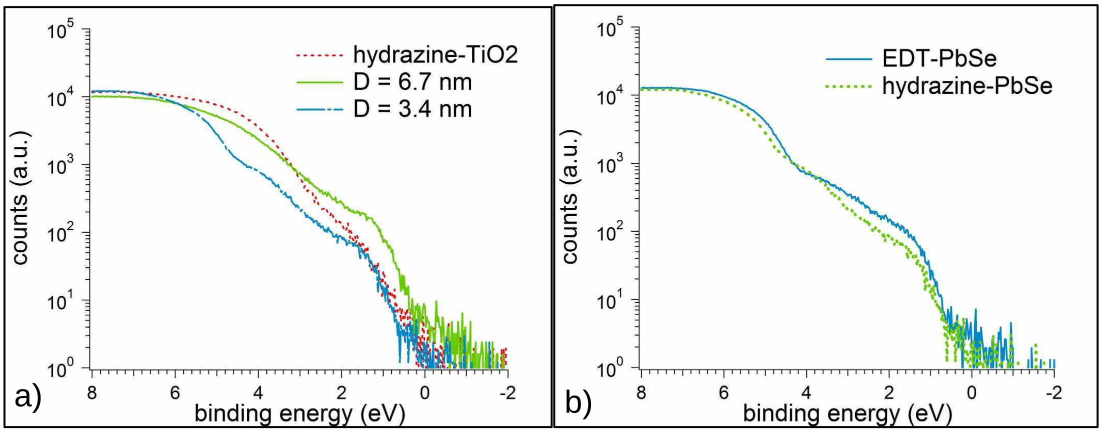

Figure 4-6. Valence region of UP spectra showing effects of ligand treatments of sub-monolayer PbSe quantum dot films on TiO_2 (110). Panel a) shows energy alignment on TiO_2 as a function of quantum dot size for hydrazine-treated PbSe with D = 6.7 nm and 3.4 nm. The substrate (dotted) trace consists of a TiO_2 (110) crystal dipped in 1 M hydrazine in acetonitrile for 23 minutes. Panel b) displays a comparison between treatment with EDT and hydrazine for 3.4 nm PbSe nanoparticles on TiO_2 (110).

ligand treatments, as illustrated in Fig. 4-6 b). The HOMO for hydrazine-treated PbSe quantum dot films on TiO_2 is 0.9 eV, and the HOMO for EDT-treated films is 0.8 eV. This shift of 0.1 eV is close to the energy resolution of the experiment and at least half the size of the quantum dot HOMO shift observed on ZnO. Second, the position of the HOMO shows a weaker dependence on quantum dot surface coverage (changing by only 0.1 eV, and in the case of hydrazine-treated films on TiO_2 the higher coverage sample exhibits a lower HOMO of 0.8 eV), indicating that the notion of an “interface” HOMO value may not be relevant in the TiO_2 systems. Also, the large enhancement of valence band intensity detected in the EDT-treated films of PbSe on ZnO ($10\bar{1}0$), attributed to improvement of nanoparticle-substrate electronic coupling through the EDT ligand molecule, is not observed on TiO_2.

The much weaker affect of the ligand treatments on the valence electronic structure of the TiO_2 substrate is confirmed by UP spectra of bare and ligand exposed TiO_2 (110) crystals (not shown). It is striking how little the density of states intensity profile is modified after ligand treatment, especially considered in relation to the changes observed for ZnO ($10\bar{1}0$) in Figures 4-1 a) and 4-4 a). Hydrazine-treated TiO_2 has a VBM unchanged from untreated TiO_2 of 2.7 eV, while EDT-treated TiO_2 has a VBM of 2.6 eV, which could possibly be due to obstruction of the underlying TiO_2 VBM by adsorbed EDT. Though, no obvious feature due to thiol adsorption is seen, in stark contrast to EDT-treated ZnO in Fig. 4-4 a), indicating that the amount of EDT on the TiO_2 (110) surface is very slight.

Finally, the work functions measured for ligand-treated PbSe quantum dot films on TiO_2 (110) show additional corroboration for the weaker nanoparticle-substrate interactions within these systems. The average work function of hydrazine-treated films on TiO_2 is 3.6 ± 0.1 eV, which represents a larger shift from the work function value of the bare substrate (3.8 eV) than was observed for hydrazine-treated films on ZnO by 0.1 eV. This shift could reflect different bonding interactions between the quantum dot and substrate, such that the stronger interactions present on the ZnO substrate lead to a stronger attractive surface potential for the outgoing photoelectrons, though the absolute work function shift between the substrates is quite small. EDT-treated films on TiO_2 had an average work function of 3.9 ± 0.1 eV, which is only half of the increase observed for EDT-treated films on ZnO. This smaller work function shift reflects the lower concentration of EDT molecules in the TiO_2 samples. Indeed, the thiol feature around 3 eV is barely detectable in the solid trace of an EDT-treated film of 3.4 nm PbSe quantum dots in Fig. 4-6 b).

The interfacial energy alignment for all of the experimental systems examined in the present work is summarized in Figure 4-7. Panel a) shows the alignment determined on ZnO ($10\bar{1}0$) substrates, while panel b) consists of the equivalent measurements on TiO_2 (110) crystals. Dotted and dashed markers for quantum dot HOMO and LUMO levels, as well as vacuum levels, correspond to hydrazine-treated and EDT-treated samples, respectively. The listed PbSe quantum dot HOMO binding energies are referenced to the Fermi level. The vacuum level shifts for each ligand treatment are shown; however,

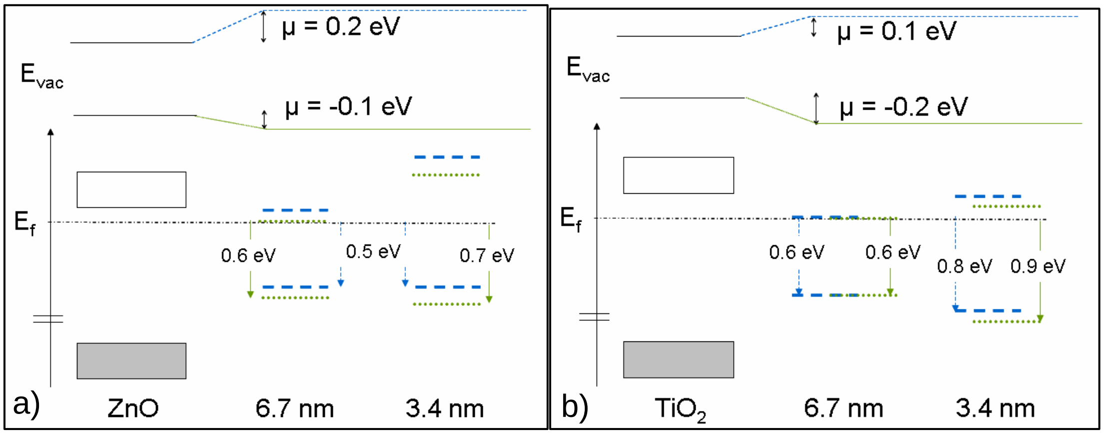

Figure 4-7. Composite energy diagrams summarizing the measured energy alignment at interfaces of EDT- and hydrazine-treated D = 6.7 nm and 3.4 nm PbSe quantum dots with (a) ZnO $(10\bar{1}0)$ substrates and (b) TiO_2 (110) substrates. The dashed markers represent EDT-treated samples, while dotted markers correspond to hydrazine-treated samples. The quantum dot HOMO binding energies displayed are referenced to E_f. The double bars on the energy axes represent a scale discontinuity. The vacuum level shifts between the two ligand treatments are offset for clarity.

they are offset on the energy axis for clarity. As was discussed earlier, the vacuum level shifts generally are caused by several contributions. The assumption equating the vacuum level offset with an interface dipole μ probably results in an overestimation of the magnitude of interfacial dipoles in these systems.

The position of the quantum dot HOMO was found to be virtually independent of size for both hydrazine- and EDT-treated films of PbSe quantum dots on ZnO; however, an absolute shift of 0.2 eV is observed between the two ligand treatments, as illustrated by the energy diagram in Fig. 4-7 a). The shift in energetic alignment at the ZnO $(10\bar{1}0)$ surface observed between the two ligand treatments is believed to result from the interactions of the ligand molecules with the ZnO substrate. As was discussed above, the ligand treatments modify the electronic structure of the ZnO substrate, but in different ways. The hydrazine treatment was found to reduce the ZnO substrate, blurring out the valence band edge in the density of states, without being incorporated to the surface, while the EDT ligand was found to strongly bind to the ZnO surface. It was suggested that EDT molecules act as molecular linkers between the PbSe quantum dots and ZnO substrate, mediating the electronic interaction, leading to wavefunction delocalization between the two semiconductors and causing enhancement of PbSe quantum dot valence band intensity.

Combining the measured HOMO positions with optical gaps allows for determination of conduction level offsets for ligand-treated PbSe quantum dots on the ZnO $(10\bar{1}0)$ substrate. The CBM of ZnO is 0.2 eV above the Fermi level.

For D = 6.7 nm PbSe quantum dots, the measured alignment places the LUMO level below the substrate CBM by 0.2 eV and 0.1 eV for hydrazine-treated and EDT-treated PbSe nanoparticles, respectively. This implies that higher-lying excited states will be needed for electron injection into ZnO. For D = 3.4 nm PbSe particles, the LUMO levels are 0.2 eV and 0.4 eV above the CBM of ZnO for hydrazine- and EDT-treated samples, respectively, suggesting that electrons in the PbSe quantum dot LUMO would have an interfacial energy gradient for charge injection into ZnO. Inclusion of the approximate interface dipoles in this alignment picture augments the conclusions reached using the measured valence band offsets. Hydrazine-treated samples show an upward vacuum level shift (0.1 eV) on crossing the interface from the PbSe quantum dot to the ZnO substrate; this can be imagined as a dipole oriented to oppose electron transfer. In contrast, a downward vacuum level shift of 0.2 eV occurs for EDT-treated PbSe quantum dots on ZnO, and this dipole would be oriented to favor electron transfer to ZnO. However, the measured vacuum level offsets cannot be simply added to the valence level offsets; rather, they offer subtle insight into the interactions observed at these interfaces.

The interfacial energy alignment measured on the TiO_2 (110) substrate generally predicts less favorable offsets with ligand-treated PbSe quantum dots, as shown in Figure 4-7 b). The VBM of the TiO_2 substrate was measured to be at 2.7 eV, and the rutile phase has a band gap of 3.0 eV. Combining these values with measured quantum dot HOMO levels from UPS and quantum dot optical transition energies leads to the energy diagram shown in Fig. 4-7 b). For both sizes of hydrazine-treated PbSe quantum dots the exciton-stabilized LUMO is below the estimated position of the TiO_2 CBM, about 0.3 eV above the Fermi level. For D = 6.7 nm EDT-treated PbSe particles on a TiO_2 substrate the PbSe quantum dot LUMO is just below the TiO_2 CBM, while the LUMO of D = 3.4 nm particles is estimated to be isoenergetic with the substrate CBM. These valence level offsets indicate that electron injection from the PbSe quantum dot LUMO to the conduction band of TiO_2 would only be possible for EDT-treated 3.4 nm PbSe quantum dots, with other systems requiring the involvement of higher-lying PbSe excited states. The directions of the vacuum level offsets, or orientation of the interfacial dipoles, at interfaces with the TiO_2 (110) substrate are the same as discussed above for ZnO $(10\bar{1}0)$ surfaces. Though the magnitudes of the vacuum level shifts are slightly different for the two different substrates, they are not expected to be quantitative measurements of the strength of interface dipoles in these systems and are considered in terms of qualitative contributions to the measured energy alignment. Nonetheless, the results of interfacial energy alignment determined from this work suggest that in order for ligand-treated PbSe quantum dots to effectively photosensitize wide band gap semiconductors such as ZnO or TiO_2, electronic states above the quantum dot LUMO must be involved with interfacial charge separation.

4.7 Conclusions

In summary, UPS was used to investigate the interfacial energetic alignment for ligand-treated colloidal PbSe quantum dot films on single crystal wide band gap oxides as a function of quantum dot size, ligand treatment, and substrate composition. The two substrates, ZnO ($10\bar{1}0$) and TiO_2 (110), showed very different behavior in directing the energy alignment with the quantum dot overlayers, and it was concluded that this difference is due mainly to the stronger affect of the ligand treatments on the valence electronic structure of the ZnO substrate. A very small shift of quantum dot HOMO (0.1 eV) with respect to changing dot size was observed for hydrazine-treated PbSe-ZnO samples, indicating that most of the (0.5 eV) band gap shift would affect the LUMO position with respect to substrate energy levels. No shift of the quantum dot HOMO was observed with changing dot size for EDT-treated PbSe-ZnO samples. Hydrazine treatment of the ZnO substrate was seen to reduce surface oxygen and erode the valence band edge, possibly enhancing reactivity toward the ligand-stripped quantum dots. EDT was found to bind strongly to the ZnO substrate, acting as a molecular linker between the quantum dots and the surface, mediating electronic coupling and causing significant enhancement of the quantum dot valence band intensity in EDT-treated films. An absolute shift in quantum dot HOMO of 0.2 eV was measured between hydrazine and EDT treatments on ZnO ($10\bar{1}0$), with EDT-treated samples displaying improved energy alignment with the ZnO substrate. In contrast to the ZnO systems, ligand treatments were seen to have very little effect on the valence band electronic structure of TiO_2 substrates, and no enhancement of quantum dot valence band intensity occurred for EDT-treated PbSe quantum dot films on TiO_2. Size-dependence of the quantum dot HOMO was observed for both ligand treatments on TiO_2 substrates, in accord with the different band gap of the quantum dots, and the quantum dot HOMO shift between the two ligand treatments on TiO_2 is much smaller than observed for ZnO samples. The determined alignment leads to prediction of poor efficiency for electron injection from quantum dot LUMO levels to the TiO_2 substrate.

In all cases the LUMO levels of the larger PbSe quantum dots (D = 6.7 nm) are below the CBM of the substrate, while most of the LUMO levels of the smaller PbSe particles (D = 3.4 nm) are at or above the CBM of the substrate, excepting hydrazine-treated PbSe on TiO_2, for which the LUMO is just below the CBM of TiO_2. These valence level offsets suggest that higher-lying excited states in PbSe quantum dots will be necessary for charge separation at interfaces with ZnO and TiO_2. On both substrates, hydrazine treatments lead to a negative vacuum level shift at the interface, while EDT treatments lead to a positive vacuum level offset. The measured vacuum level shifts were considered in the context of interface dipoles that would either reinforce or oppose the valence level offsets. These findings indicate that the different degree of ligand interaction with the oxide substrate is primarily responsible for the different quantum dot-substrate electronic interactions, and, consequently, the different interfacial energy alignment observed here.

4.8 References

1. Murphy, J. E.; Beard, M. C.; Nozik, A. J., *J. Phys. Chem. B* **2006**, *110*, 25455-25461.
2. Moreels, I.; Lambert, K.; De Muynck, D.; Vanhaecke, F.; Poelman, D.; Martins, J. C.; Allan, G.; Hens, Z., *Chem. Mater.* **2007,** *19,* 6101–6106.
3. Schaller, R. D.; Klimov, V. I., *Phys. Rev. Lett.* **2004**, *92*, 186601(4).
4. Ellingson, R. J.; Beard, M. C.; Johnson, J. C.; Yu, P.-R.; Micic, O. I.; Nozik, A. J.; Shabaev, A.; Efros, A. L., *Nano Lett.* **2005**, *5*, 865-871.
5. Cui, D.; Xu, J.; Zhu, T.; Paradee, G.; Ashok, S.; Gerhold, M., *Appl. Phys. Lett.* **2006**, *88*, 183111(3).
6. Jiang, X.-M.; Schaller, R. D.; Lee, S. B.; Pietryga, J. M.; Klimov, V. I.; Zakhidov, A. A., *J. Mater. Res.* **2007**, *22*, 2204-2210.
7. Aldana, J.; Wang, Y. A.; Peng, X.-G., *J. Am. Chem. Soc.* **2001**, *123*, 8844-8850.
8. Luther, J. M.; Law, M.; Beard, M. C.; Song, Q.; Reese, M. O.; Ellingson, R. J.; Nozik, A. J., *Nano Lett.* **2008**, *8*, 3488-3492.
9. Koleilat, G. I.; Levina, L.; Shukla, H.; Myrskog, S. H.; Hinds, S.; Pattantyus-Abraham, A. G.; Sargent, E. H., *ACS Nano* **2008**, *2*, 833-840.
10. Talapin, D. V.; Murray, C. B., *Science* **2005**, *310*, 86-89.
11. Barkhouse, D. A. R.; Pattantyus-Abraham, A. G.; Levina, L.; Sargent, E. H., *ACS Nano* **2008**, 2, 2356-2362.

12. Law, M.; Luther, J. M.; Song, Q.; Hughes, B. K.; Perkins, C. L.; Nozik, A. J., *J. Am. Chem. Soc.* **2008**, *130*, 5974-5985.
13. Leschkies, K. S.; Divakar, R.; Basu, J.; Enache-Pommer, E.; Boercker, J. E.; Carter, C. B.; Kortshagen, U. R.; Norris, D. J.; Aydil, E. S., *Nano Lett.* **2007**, *7*, 1793-1798.
14. Lpez-Luke, T.; Wolcott, A.; Xu, L.-P.; Chen, S.-W.; Wen, Z.-H.; Li, J.-H.; De La Rosa, E.; Zhang, J. Z., *J. Phys. Chem. C* **2008**, *112*, 1282-1292.
15. Bang, J. H.; Kamat, P. V., *ACS Nano*, **2009**, *3*, 1467-1476.
16. Lee, H. J.; Chem, P.; Moon, S.-J.; Sauvage, F.; Sivula, K.; Bessho, T.; Gamelin, D. R.; Comte, P.; Zakeeruddin, S. M.; Seok, S. I.; Grätzel, M.; Nazeeruddin, M. K., *Langmuir* **2009**, *25*, 7602–7608.
17. Cao, X.; Chen, P.; Guo, Y., *J. Phys. Chem. C* **2008,** *112,* 20560–20566.
18. Zaban, A.; Micic, O. I.; Gregg, B. A.; Nozik, A. J., *Langmuir* **1998,** *14,* 3153-3156.
19. Yu, P.-R.; Zhu, K.; Norman, A. G.; Ferrere, S.; Frank, A. J.; Nozik, A. J., *J. Phys. Chem. B* **2006,** *110,* 25451-25454.
20. Hyun, B.-R.; Zhong, Y.-W.; Bartnik, A. C.; Sun, L.-F.; Abruna, H. D.; Wise, F. W.; Goodreau, J. D.; Matthews, J. R.; Leslie, T. M.; Borrelli, N. F., *ACS Nano* **2008**, *2*, 2206-2212.
21. Vogel, R.; Hoyer, P.; Weller, H., *J. Phys. Chem.* ***1994***, *98,* 3183-3188.
22. Wang, C.-J.; Kwon, K.-W.; Odlyzko, M. L.; Lee, B. H.; Shim, M., *J. Phys. Chem. C* **2007,** *111,* 11734-11741.

23. Robel, I.; Kuno, M.; Kamat, P. V., *J. Am. Chem. Soc.* **2007**, *129*, 4136-4137.
24. Hoyer, P.; Könenkamp, R., *Appl. Phys. Lett.* **1995**, *66*, 349-351.
25. Franceschetti, A., *Phys. Rev. B* **2008**, *78*, 075418(6).
26. Ishii, H.; Sugiyama, K.; Ito, E.; Seki, K., *Adv. Mater.* **1999**, *11*, 605-625.
27. Horn, K., *Appl. Phys. A* **1990**, *51*, 289-304.
28. Liu, G.-M.; Klein, A.; Thissen, A.; Jaegermann, W., *Surf. Sci.* **2003**, *539*, 37-48.
29. Snook, J. H.; Samuelson, L. A.; Kumar, J.; Kim, Y.-G.; Whitten, J. E., *Organic Electronics* **2005**, *6*, 55–64.
30. Shimada, T.; Kaji, T.; Saiki, K., *Mol. Cryst. Liq. Cryst.* **2006**, *455*, 317-325.
31. Carlson, B.; Leschkies, K.; Aydil, E. S.; Zhu, X.-Y., *J. Phys. Chem. C* **2008,** *112,* 8419–8423.
32. Shalom, M.; Rühle, S.; Hod, I.; Yahav, S; Zaban, A., *J. Am. Chem. Soc.* **2009**, *131*, 9876-9877.
33. Luther, J. M.; Law, M.; Song, Q.; Perkins, C. L.; Beard, M. C.; Nozik, A. J., *ACS Nano* **2008**, *2*, 271-280.
34. Dai, Q.; Wang, Y.-N.; Li, X.; Zhang, Y.; Pellegrino, D. J.; Zhao, M.; Zou, B.; Seo, J.-T.; Wang, Y.; Yu, W. W., *ACS Nano* **2009**, *3*, 1518-1524.
35. Lu, Y.-F.; Jaeckel, B.; Parkinson, B. A., *Langmuir* **2006**, *22*, 4472-4475.
36. Williams, K. J.; Tisdale, W. A.; Leschkies, K. S.; Haugstad, G.; Norris, D. J., Aydil, E. S.; Zhu, X.-Y., *ACS Nano* **2009**, *3*, 1532-1538.

37. Ulman, A., *Chem. Rev.* **1996,** *96*, 1533-1554.
38. Ozawa, K.; Sawada, K. Shirotori, Y.; Edamoto, K., *J. Phys.: Condens. Matter* **2005**, *17*, 1271–1278.
39. Imanishi, A.; Tsuji, E.; Nakato, Y., *J. Phys. Chem. C* **2007**, *111*, 2128-2132.
40. Lüth, H.; Rubloff, G. W.; Grobman, W. D., *Solid State Comm.* **1976**, *18*, 1427-1430.
41. Wang, L.; Chen, S.; Liu, L.; Qi, D.-C.; Gao, X.-Y.; Wee, A. T. S., *Appl. Phys. Lett.* **2007**, *90*, 132121(3).
42. Hummer, K.; Grüneis, A.; Kresse, G., *Phys. Rev. B* **2007**, *75*, 195211(9).
43. An, J. M.; Franceschetti, A.; Dudiy, S. V.; Zunger, A., *Nano Lett.* **2006**, *6*, 2728-2735.
44. Kang, I.; Wise, F. W., *J. Opt. Soc. Am. B* **1997**, *14*, 1632-1646.
45. Ahn, H.; Kim, M.; Sandman, D. J.; Whitten, J. E., *Langmuir* **2003,** *19,* 5303-5310.
46. Lahiri, J.; Batzill, M., *J. Phys. Chem. C* **2008**, *112*, 4304-4307.
47. Young, A. G.; Green, D. P.; McQuillan, A. J., *Langmuir* **2006,** *22*, 11106-11112.

Bibliography

Chapter 1

1. Gregg, B. A., *J. Phys. Chem. B* **2003**, *107*, 4688-4698.
2. O'Regan, B.; Grätzel, M., *Nature* **1991**, *353*, 737-740.
3. Green, M. A., *Prog. Photovolt: Res. Appl.* **2001**, *9*, 123-135.
4. Nozik, A. J., *Physica E* **2002**, *14*, 115-120.
5. Nozik, A. J., *Chem. Phys. Lett.* **2008**, *457*, 3-11.
6. Kim, J. Y.; Lee, K.; Coates, N. E.; Moses, D.; Nguyen, T.-Q.; Dante, M.; Heeger, A. J., *Science* **2007**, *317*, 222-225.
7. Vogel, R.; Pohl, K.; Weller, H., *Chem. Phys. Lett.* **1990**, *174*, 241-246.
8. Liu, D.; Kamat, P. V., *J. Phys. Chem.* ***1993***, *97*, 10769-10773.
9. Vogel, R.; Hoyer, P.; Weller, H., *J. Phys. Chem.* **1994**, *98*, 3183-3188.
10. Hoyer, P.; Könenkamp, R., *Appl. Phys. Lett.* **2005**, *66*, 349-351.
11. Murray, C. B.; Norris, D. J.; Bawendi, M. G., *J. Am. Chem. Soc.* **1993**, *115*, 8706-8715.
12. Puzder, A.; Williamson, A. J.; Zaitseva, N.; Galli, G.; Manna, L.; Alivisatos, A. P., *Nano Lett.* **2004**, *4*, 2361-2365.
13. Lawless, D.; Kapoor, S.; Meisel, D., *J. Phys. Chem.* **1995**, *99*, 10329-10335.
14. Robel, I.; Subramanian, V.; Kuno, M.; Kamat, P. V., *J. Am. Chem. Soc.* **2006**, *128*, 2385-2393.

15. Leschkies, K. S.; Divakar, R.; Basu, J.; Enache-Pommer, E.; Boercker, J. E.; Carter, C. B.; Kortshagen, U. R.; Norris, D. J.; Aydil, E. S., *Nano Lett.* **2007**, *7*, 1793-1798.
16. Cao, X.; Chen, P.; Guo, Y., *J. Phys. Chem. C* **2008**, *112*, 20560-20566.
17. Yu, P.-R.; Zhu, K.; Norman, A. G.; Ferrere, S.; Frank, A. J.; Nozik, A. J., *Langmuir* **1998**, *14*, 3153-3156.
18. Murphy, J. E.; Beard, M. C.; Nozik, A. J., *J. Phys. Chem. B* **2006**, *110*, 25455-25461.
19. Hyun, B.-R.; Zhong, Y.-W.; Bartnik, A. C.; Sun, L.-F.; Abruna, H. D.; Wise, F. W.; Goodreau, J. D.; Matthews, J. R.; Leslie, T. M.; Borrelli, N. F., *ACS Nano* **2008**, *2*, 2206-2212.
20. Aldana, J.; Wang, Y. A.; Peng, X.-G., *J. Am. Chem. Soc.* **2001**, *123*, 8844-8850.
21. Moody, I. S.; Stonas, A. R.; Lonergan, M. C., *J. Phys. Chem. C* **2008**, *112*, 19383-19389.
22. Frank, A. J.; Kopidakis, N.; van de Lagemaat, J., *Coord. Chem. Rev.* **2004**, *248*, 1165-1179.
23. Law, M.; Greene, L. E.; Johnson, J. C.; Saykally, R.; Yang, P., *Nat. Mater.* **2005**, *4*, 455-459.
24. Baxter, J. B.; Walker, A. M.; van Ommering, K.; Aydil, E. S., *Nanotech.* **2006**, *17*, S304-S312.
25. Kamat, P. V., *J. Phys. Chem. C* **2007**, *111*, 2834-2860.
26. Liu, B.; Aydil, E. S., *J. Am. Chem. Soc.* **2009**, *131*, 3985-3990.

27. Kongkanand, A.; Tvrdy, K.; Takechi, K.; Kuno, M.; Kamat, P. V., *J. Am. Chem. Soc.* **2008**, *130*, 4007-4015.
28. Klem, E. J. D.; MacNeil, D. D.; Lavina, L.; Sargent, E. H., *Adv. Mater.* **2008**, *20*, 3433-3439.
29. Luther, J. M.; Law, M.; Beard, M. C.; Song, Q.; Reese, M. O.; Ellingson, R. J.; Nozik, A. J., *Nano Lett.* **2008**, *8*, 3488-3492.
30. Koleilat, G. I.; Levina, L.; Shukla, H.; Myrskog, S. H.; Hinds, S.; Pattantyus-Abraham, A. G.; Sargent, E. H., *ACS Nano* **2008**, *2*, 833-840.
31. Liljeroth, P.; Overgaag, K.; Urbieta, A.; Grandidier, B.; Hickey, S. G.; Vanmaekelbergh, D., *Phys. Rev. Lett.* **2006**, *97*, 096803(4).
32. Talapin, D. V.; Murray, C. B., *Science* **2005**, *310*, 86-89.
33. Law, M.; Luther, J. M.; Song, Q.; Hughes, B. K.; Perkins, C. L.; Nozik, A. J., *J. Am. Chem. Soc.* **2008**, *130*, 5974-5985.
34. Luther, J. M.; Law, M.; Song, Q.; Perkins, C. L.; Beard, M. C.; Nozik, A. J., *ACS Nano* **2008**, *2*, 271-280.
35. Wang, L.-W.; Zunger, A., *Phys. Rev. B* **1996**, *53*, 9579(4).
36. Karazhanov, S. Zh.; Lew Yan Voon, L. C., *Semiconductors* **2005**, *39*, 161-173.
37. Jdira, L., Liljeroth, P.; Stoffels, E.; Vanmaekelbergh, D., Speller, S., *Phys. Rev. B* **2006**, *73*, 115305(6).
38. Meulenberg, R. W.; Lee, J. R. I.; Wolcott, A.; Zhang, J. Z.; Terminello, L. J., van Buuren, T., *ACS Nano* **2009**, *3*, 325-330.

39. Inamdar, S. M.; Ingole, P. P.; Haram, S. K., *ChemPhysChem* **2008**, *9*, 2574-2579.
40. Guyot-Sionnest, P.; Wehrenberg, B.; Yu, D., *J. Chem. Phys.* **2005**, *123*, 074709(7).
41. Kippeny, T. C.; Bowers, M. J.; Dukes, A. D.; McBride, J. R.; Orndorff, R. L.; Garrett, M. D.; Rosenthal, S. J., *J. Chem. Phys.* **2008**, *128*, 084713(7).
42. Wuister, S. F.; de Mello Donegá, C.; Meijerink, A., *J. Phys. Chem. B* **2004**, *108*, 17393-17397.
43. Pokrant, S.; Whaley, K. B., *Eur. Phys. J. D* **1999**, *6*, 255-267.
44. Puzder, A.; Williamson, A. J.; Gygi, F.; Galli, G., *Phys. Rev. Lett.* **2004**, *92*, 217401(4).
45. Alperson, B.; Rubinstein, I.; Hodes, G., *Phys. Rev. B* **2001**, *63*, 081303(4).
46. Bowen Katari, J. E.; Colvin, V. L.; Alivisatos, A. P., *J. Phys. Chem.* **1994**, *98*, 4109-4117.
47. Taylor, J.; Kippeny, T.; Rosenthal, S. J., *J. Cluster Sci.* **2002**, *12*, 571-582.
48. Murray, C. B.; Sun, S.-H., Gaschler, W.; Doyle, H.; Betley, T. A.; Kagan, C. R., *IBM J. Res. & Dev.* **2001**, *45*, 47-56.
49. Schaller, R. D.; Klimov, V. I., *Phys. Rev. Lett.* **2004**, *92*, 186601(4).
50. Wise, F. W., *Acc. Chem. Res.* **2000**, *33*, 773-780.

51. Wehrenberg, B. L.; Guyot-Sionnest, P., *J. Am. Chem. Soc.* **2003**, *125*, 7806-7807.
52. Franceschetti, A., *Phys. Rev. B* **2008**, *78*, 075418(6).
53. Mentzel, T. S.; Porter, V. J.; Geyer, S.; MacLean, K.; Bawendi, M. G.; Kastner, M. A., *Phys. Rev. B* **2008**, *77*, 075316(8).
54. Hummer, K.; Grüneis, A.; Kresse, G., *Phys. Rev. B* **2007**, *75*, 195211(9).
55. Harbold, J. M.; Wise, F. W., *Phys. Rev. B* **2007**, *76*, 125304(6).
56. An, J. M.; Franceschetti, A.; Dudiy, S. V.; Zunger, A., *Nano Lett.* **2006**, *6*, 2728-2735.
57. Kim, D. I.; Islam, M. A.; Avila, L.; Herman, I. P., *J. Phys. Chem. B* **2003**, *107*, 6318-6323.
58. Steiner, D.; Aharoni, A.; Banin, U.; Millo, O., *Nano Lett.* **2006**, *6*, 2201-2205.
59. Liljeroth, P.; Zeijlmans van Emmichoven, P. A.; Hickey, S. G.; Weller, H.; Grandidier, B.; Allan, G.; Vanmaekelbergh, D., *Phys. Rev. Lett.* **2005**, *95*, 086801(4).
60. Williams, K. J.; Tisdale, W. A.; Leschkies, K. S.; Haugstad, G.; Norris, D. J., Aydil, E. S.; Zhu, X.-Y., *ACS Nano* **2009**, *3*, 1532-1538.
61. Allan, G.; Delerue, C., *Phys. Rev. B* **2004**, *70*, 245321(9).
62. Moreels, I.; Lambert, K.; De Muynck, D.; Vanhaecke, F.; Poelman, D.; Martins, J. C.; Allan, G.; Hens, Z., *Chem. Mater.* **2007,** *19,* 6101–6106.
63. Dai, Q.; Wang, Y.-N.; Li, X.; Zhang, Y.; Pellegrino, D. J.; Zhao, M.; Zou, B.; Seo, J.-T.; Wang, Y.; Yu, W. W., *ACS Nano* **2009**, *3*, 1518-1524.

64. Moreels, I.; Fritzinger, B.; Martins, J. C.; Hens, Z., *J. Am. Chem. Soc.* **2008**, *130*, 15081-15086.

Chapter 2

1. Onda, K.; Li, B.; Petek, H., *Phys. Rev. B* **2004**, *70*, 045415(11).
2. Diebold, U.; Koplitz, L. V.; Dulub, O., *Appl. Surf. Sci.* **2004**, *237*, 336-342.
3. Leschkies, K. S.; Divakar, R.; Basu, J.; Enache-Pommer, E.; Boercker, J. E.; Carter, C. B.; Kortshagen, U. R.; Norris, D. J.; Aydil, E. S., *Nano Lett.* **2007**, *7*, 1793-1798.
4. Reiss, P.; Bleuse, J.; Pron, A., *Nano Lett.* **2002**, *2*, 781-784.
5. Yu, W. W.; Qu, L.-H.; Guo, W.-Z.; Peng, X.-G., *Chem. Mater.* **2003**, *15*, 2854-2860.
6. Aldana, J.; Wang, Y. A.; Peng, X.-G., *J. Am. Chem. Soc.* **2001**, *123*, 8844-8850.
7. Murphy, J. E.; Beard, M. C.; Nozik, A. J., *J. Phys. Chem. B* **2006**, *110*, 25455-25461.
8. Luther, J. M.; Law, M.; Song, Q.; Perkins, C. L.; Beard, M. C.; Nozik, A. J., *ACS Nano* **2008**, *2*, 271-280.
9. Dai, Q.; Wang, Y.-N.; Li, X.; Zhang, Y.; Pellegrino, D. J.; Zhao, M.; Zou, B.; Seo, J.-T.; Wang, Y.; Yu, W. W., *ACS Nano* **2009**, *3*, 1518-1524.
10. Lu, Y.-F.; Jaeckel, B.; Parkinson, B. A., *Langmuir* **2006**, *22*, 4472-4475.

11. Williams, K. J.; Tisdale, W. A.; Leschkies, K. S.; Haugstad, G.; Norris, D. J., Aydil, E. S.; Zhu, X.-Y., *ACS Nano* **2009**, *3*, 1532-1538.
12. Braun, S.; Osikowicz, W.; Wang, Y.; Salaneck, W. R., *Organic Electronics* **2007**, *8*, 14-20.
13. Tang, J. X.; Lee, C. S.; Lee, S. T., *J. Appl. Phys.* **2007**, *101*, 064504(4).
14. Alperson, B.; Rubinstein, I.; Hodes, G., *Phys. Rev. B* **2001**, *63*, 081303(4).
15. Meulenberg, R. W.; Lee, J. R. I.; Wolcott, A.; Zhang, J. Z.; Terminello, L. J., van Buuren, T., *ACS Nano* **2009**, *3*, 325-330.
16. Kang, I.; Wise, F. W., *J. Opt. Soc. Am. B* **1997**, *14*, 1632-1646.

Chapter 3

1. Gregg, B. A., *J. Phys. Chem. B* **2003**, *107*, 4688-4698.
2. O'Regan, B.; Grätzel, M., *Nature* **1991**, *353*, 737-740.
3. Baxter, J. B.; Aydil, E. S., *Appl. Phys. Lett.* **2005**, *86*, 053114(3).
4. Law, M.; Greene, L. E.; Johnson, J. C.; Saykally, R.; Yang, P., *Nat. Mater.* **2005**, *4*, 455-459.
5. Vogel, R.; Pohl, K.; Weller, H., *Chem. Phys. Lett.* **1990**, *174*, 241-246.
6. Vogel, R.; Hoyer, P.; Weller, H., *J. Phys. Chem.* **1994**, *98*, 3183-3188.
7. Yu, P.-R.; Zhu, K.; Norman, A. G.; Ferrere, S.; Frank, A. J.; Nozik, A. J., *Langmuir* **1998**, *14*, 3153-3156.

8. Leschkies, K. S.; Divakar, R.; Basu, J.; Enache-Pommer, E.; Boercker, J. E.; Carter, C. B.; Kortshagen, U. R.; Norris, D. J.; Aydil, E. S., *Nano Lett.* **2007**, *7*, 1793-1798.
9. Robel, I.; Subramanian, V.; Kuno, M.; Kamat, P. V., *J. Am. Chem. Soc.* **2006**, *128*, 2385-2393.
10. Liu, D.; Kamat, P. V., *J. Phys. Chem.* ***1993***, *97*, 10769-10773.
11. Schaller, R. D.; Klimov, V. I., *Phys. Rev. Lett.* **2004**, *92*, 186601(4).
12. Ellingson, R. J.; Beard, M. C.; Johnson, J. C.; Yu, P.-R.; Micic, O. I.; Nozik, A. J.; Shabaev, A.; Efros, A. L., *Nano Lett.* **2005**, *5*, 865-871.
13. Olson, D. C.; Piris, J.; Collins, R. T.; Shaheen, S. E.; Ginley, D. S., *Thin Solid Films* **2006**, *496*, 26-29.
14. Diebold, U.; Koplitz, L. V.; Dulub, O., *Appl. Surf. Sci.* **2004**, *237*, 336-342.
15. Colvin, V. L.; Alivisatos, A. P.; Tobin, J. G., *Phys. Rev. Lett.* **1991**, *66*, 2786-2789.
16. Wu, P.-J.; Tsuei, K.-D.; Hsieh, M.-T.; Wei, K.-H.; Liang, K. S., *Phys. Rev. B* **2007**, *75*, 115402(8).
17. Lee, J. R. I.; Meulenberg, R. W.; Hanif, K. M.; Mattoussi, H.; Klepeis, J. E.; Terminello, L. J.; van Buuren, T., *Phys. Rev. Lett.* **2007**, *98*, 146803(4).
18. Reiss, P.; Bleuse, J.; Pron, A., *Nano Lett.* **2002**, *2*, 781-784.
19. Yu, W. W.; Qu, L.-H.; Guo, W.-Z.; Peng, X.-G., *Chem. Mater.* **2003**, *15*, 2854-2860.

20. Aldana, J.; Wang, Y. A.; Peng, X.-G., *J. Am. Chem. Soc.* **2001**, *123*, 8844-8850.
21. Lüth, H.; Rubloff, G. W.; Grobman, W. D., *Solid State Comm.* **1976**, *18*, 1427-1430.
22. Moulder, J. F.; Stickle, W. F.; Sobol, P. E.; Bomben, K. D.; *Handbook of X-ray Photoelectron Spectroscopy*; Physical Electronics, Inc.: Eden Prairie, 1995.
23. Ozawa, K.; Sawada, K.; Shirotori, Y.; Edamoto, K., *J. Phys.: Condens. Matter* **2005**, *17*, 1271-1278.
24. Franceschetti, A.; Zunger, A., *Phys. Rev. Lett.* **2007**, *98*, 915-918.
25. Brus, L., *J. Phys. Chem.* **1986**, *90*, 2555-2560.
26. Dalven, R., *Phys. Stat. Sol. B* **1971**, *48*, K23-K26.
27. Wang, L.-W.; Li, J., *Phys. Rev. B* **2004**, *69*, 153302(4).

Chapter 4

1. Murphy, J. E.; Beard, M. C.; Nozik, A. J., *J. Phys. Chem. B* **2006**, *110*, 25455-25461.
2. Moreels, I.; Lambert, K.; De Muynck, D.; Vanhaecke, F.; Poelman, D.; Martins, J. C.; Allan, G.; Hens, Z., *Chem. Mater.* **2007,** *19,* 6101–6106.
3. Schaller, R. D.; Klimov, V. I., *Phys. Rev. Lett.* **2004**, *92*, 186601(4).
4. Ellingson, R. J.; Beard, M. C.; Johnson, J. C.; Yu, P.-R.; Micic, O. I.; Nozik, A. J.; Shabaev, A.; Efros, A. L., *Nano Lett.* **2005**, *5*, 865-871.

5. Cui, D.; Xu, J.; Zhu, T.; Paradee, G.; Ashok, S.; Gerhold, M., *Appl. Phys. Lett.* **2006**, *88*, 183111(3).
6. Jiang, X.-M.; Schaller, R. D.; Lee, S. B.; Pietryga, J. M.; Klimov, V. I.; Zakhidov, A. A., *J. Mater. Res.* **2007**, *22*, 2204-2210.
7. Aldana, J.; Wang, Y. A.; Peng, X.-G., *J. Am. Chem. Soc.* **2001**, *123*, 8844-8850.
8. Luther, J. M.; Law, M.; Beard, M. C.; Song, Q.; Reese, M. O.; Ellingson, R. J.; Nozik, A. J., *Nano Lett.* **2008**, *8*, 3488-3492.
9. Koleilat, G. I.; Levina, L.; Shukla, H.; Myrskog, S. H.; Hinds, S.; Pattantyus-Abraham, A. G.; Sargent, E. H., *ACS Nano* **2008**, *2*, 833-840.
10. Talapin, D. V.; Murray, C. B., *Science* **2005**, *310*, 86-89.
11. Barkhouse, D. A. R.; Pattantyus-Abraham, A. G.; Levina, L.; Sargent, E. H., *ACS Nano* **2008**, 2, 2356-2362.
12. Law, M.; Luther, J. M.; Song, Q.; Hughes, B. K.; Perkins, C. L.; Nozik, A. J., *J. Am. Chem. Soc.* **2008**, *130*, 5974-5985.
13. Leschkies, K. S.; Divakar, R.; Basu, J.; Enache-Pommer, E.; Boercker, J. E.; Carter, C. B.; Kortshagen, U. R.; Norris, D. J.; Aydil, E. S., *Nano Lett.* **2007**, *7*, 1793-1798.
14. Lpez-Luke, T.; Wolcott, A.; Xu, L.-P.; Chen, S.-W.; Wen, Z.-H.; Li, J.-H.; De La Rosa, E.; Zhang, J. Z., *J. Phys. Chem. C* **2008**, *112*, 1282-1292.
15. Bang, J. H.; Kamat, P. V., *ACS Nano*, **2009**, *3*, 1467-1476.

16. Lee, H. J.; Chem, P.; Moon, S.-J.; Sauvage, F.; Sivula, K.; Bessho, T.; Gamelin, D. R.; Comte, P.; Zakeeruddin, S. M.; Seok, S. I.; Grätzel, M.; Nazeeruddin, M. K., *Langmuir* **2009**, *25*, 7602–7608.
17. Cao, X.; Chen, P.; Guo, Y., *J. Phys. Chem. C* **2008,** *112,* 20560–20566.
18. Zaban, A.; Micic, O. I.; Gregg, B. A.; Nozik, A. J., *Langmuir* **1998,** *14,* 3153-3156.
19. Yu, P.-R.; Zhu, K.; Norman, A. G.; Ferrere, S.; Frank, A. J.; Nozik, A. J., *J. Phys. Chem. B* **2006,** *110,* 25451-25454.
20. Hyun, B.-R.; Zhong, Y.-W.; Bartnik, A. C.; Sun, L.-F.; Abruna, H. D.; Wise, F. W.; Goodreau, J. D.; Matthews, J. R.; Leslie, T. M.; Borrelli, N. F., *ACS Nano* **2008**, *2*, 2206-2212.
21. Vogel, R.; Hoyer, P.; Weller, H., *J. Phys. Chem.* ***1994***, *98,* 3183-3188.
22. Wang, C.-J.; Kwon, K.-W.; Odlyzko, M. L.; Lee, B. H.; Shim, M., *J. Phys. Chem. C* **2007,** *111,* 11734-11741.
23. Robel, I.; Kuno, M.; Kamat, P. V., *J. Am. Chem. Soc.* **2007**, *129*, 4136-4137.
24. Hoyer, P.; Könenkamp, R., *Appl. Phys. Lett.* **1995**, *66*, 349-351.
25. Franceschetti, A., *Phys. Rev. B* **2008**, *78*, 075418(6).
26. Ishii, H.; Sugiyama, K.; Ito, E.; Seki, K., *Adv. Mater.* **1999**, *11*, 605-625.
27. Horn, K., *Appl. Phys. A* **1990**, *51*, 289-304.
28. Liu, G.-M.; Klein, A.; Thissen, A.; Jaegermann, W., *Surf. Sci.* **2003**, *539*, 37-48.

29. Snook, J. H.; Samuelson, L. A.; Kumar, J.; Kim, Y.-G.; Whitten, J. E., *Organic Electronics* **2005**, *6*, 55–64.
30. Shimada, T.; Kaji, T.; Saiki, K., *Mol. Cryst. Liq. Cryst.* **2006**, *455*, 317-325.
31. Carlson, B.; Leschkies, K.; Aydil, E. S.; Zhu, X.-Y., *J. Phys. Chem. C* **2008,** *112,* 8419–8423.
32. Shalom, M.; Rühle, S.; Hod, I.; Yahav, S; Zaban, A., *J. Am. Chem. Soc.* **2009**, *131*, 9876-9877.
33. Luther, J. M.; Law, M.; Song, Q.; Perkins, C. L.; Beard, M. C.; Nozik, A. J., *ACS Nano* **2008**, *2*, 271-280.
34. Dai, Q.; Wang, Y.-N.; Li, X.; Zhang, Y.; Pellegrino, D. J.; Zhao, M.; Zou, B.; Seo, J.-T.; Wang, Y.; Yu, W. W., *ACS Nano* **2009**, *3*, 1518-1524.
35. Lu, Y.-F.; Jaeckel, B.; Parkinson, B. A., *Langmuir* **2006**, *22*, 4472-4475.
36. Williams, K. J.; Tisdale, W. A.; Leschkies, K. S.; Haugstad, G.; Norris, D. J., Aydil, E. S.; Zhu, X.-Y., *ACS Nano* **2009**, *3*, 1532-1538.
37. Ulman, A., *Chem. Rev.* **1996,** *96*, 1533-1554.
38. Ozawa, K.; Sawada, K. Shirotori, Y.; Edamoto, K., *J. Phys.: Condens. Matter* **2005**, *17*, 1271–1278.
39. Imanishi, A.; Tsuji, E.; Nakato, Y., *J. Phys. Chem. C* **2007**, *111*, 2128-2132.
40. Lüth, H.; Rubloff, G. W.; Grobman, W. D., *Solid State Comm.* **1976**, *18*, 1427-1430.

41. Wang, L.; Chen, S.; Liu, L.; Qi, D.-C.; Gao, X.-Y.; Wee, A. T. S., *Appl. Phys. Lett.* **2007**, *90*, 132121(3).
42. Hummer, K.; Grüneis, A.; Kresse, G., *Phys. Rev. B* **2007**, *75*, 195211(9).
43. An, J. M.; Franceschetti, A.; Dudiy, S. V.; Zunger, A., *Nano Lett.* **2006**, *6*, 2728-2735.
44. Kang, I.; Wise, F. W., *J. Opt. Soc. Am. B* **1997**, *14*, 1632-1646.
45. Ahn, H.; Kim, M.; Sandman, D. J.; Whitten, J. E., *Langmuir* **2003,** *19,* 5303-5310.
46. Lahiri, J.; Batzill, M., *J. Phys. Chem. C* **2008**, *112*, 4304-4307.
47. Young, A. G.; Green, D. P.; McQuillan, A. J., *Langmuir* **2006,** *22*, 11106-11112.